Scraping of a thin layer of viscoplastic fluid

J. J. Taylor-West* and A. J. Hogg
School of Mathematics, University of Bristol, Bristol BS8 1QU, United Kingdom

(Received 16 January 2024; accepted 26 April 2024; published 14 May 2024)

We analyze the scraping of a thin layer of viscoplastic fluid residing on a horizontal surface by a translating rigid scraper. This motion generates a mound of fluid upstream of the scraper and a residual layer behind it, both of which are modelled using a shallow layer theory for a Bingham or Herschel-Bulkley fluid. The flows ahead of and behind the scraper are coupled by the motion in the gap under the scraper, which is driven both by the translation of the scraper and by the induced pressure gradient due to the difference in flow thickness upstream and downstream. When the gap between the scraper and the underlying surface is sufficiently small, we find that a steady state emerges after a relatively long transient and that en route to this state, the unsteady dynamics exhibit a variety of regimes that are self-similar to leading order. We construct these solutions explicitly and derive key scalings for the temporal development of the flowing viscoplastic layer, as well as identifying the timescales at which there are transitions between the regimes. These predictions are confirmed by comparison with results from the numerical integration of the full system. Finally, we report results from preliminary laboratory experiments, which are compared with predictions from the shallow-layer theory, obtaining reasonable agreement once a slip boundary condition is included in the model, as motivated by experimental observations.

DOI: 10.1103/PhysRevFluids.9.053301

I. INTRODUCTION

This study investigates the scraping of a thin layer of viscoplastic fluid from a plane surface. The flow configuration and rheology is relevant to a number of environmental and industrial processes. For example, the removal of excess plaster from a wall or of a layer of mud from a road following a mudslide may be carried out by the translation of a vertical scraper, where both of these materials are known to exhibit viscoplastic rheology [1–3]. A similar flow configuration is also relevant to blade coating and screen printing processes where the desired result is a uniform residual layer of fluid behind the scraper [4–7]. Finally, in geophysics, similar flow configurations have been used as a model for the formation of fold-and-thrust belts and accretionary wedges at converging tectonic plates, whereby a layer of relatively soft sediment is scraped off a descending plate by the more rigid overlying plate during plate subduction. Emerman and Turcotte [8] used a Newtonian rheology and shallow layer theory, identifying a late time similarity solution in which the shape of the wedge is quasistatic, although they do not explicitly determine the time dependence of the height or length of the mound in this regime. Similarly, Perazzo and Gratton [9] considered the uplift due to the

*j.taylor-west@bristol.ac.uk

convergence of two shallow layers of Newtonian fluid, identifying an early time similarity solution in which the height and length of the wedges grow with time, t, as $t^{1/2}$ and a late time similarity solution in which the height grows as $t^{1/4}$ and the length as $t^{3/4}$ (corresponding to the shape found by Emerman and Turcotte [8]). Ball *et al.* [10] considered an extension to the viscous wedge theory in which the underlying plate is modelled as an elastic beam, which introduces an additional, elastogravitational, length scale and results in the model exhibiting a number of additional dynamic regimes. Stockmal [11] and Davis *et al.* [12] studied the problem for a plastic Coulomb rheology by using shallow layer theory and slipline theory, respectively, under the assumption that the material is at failure throughout the wedge. These models result in a self-similar tapered geometry of the wedge. Fully two-dimensional finite-element simulations accounting for the free surface have also been carried out for Coulomb plastic [13] and viscoelastic-plastic [14,15] rheologies. These simulations benefit from being able to resolve heterogeneous deformation and complex surface features that are otherwise filtered out by the shallow layer approximation; in particular they predict deformation via a sequence of folds or thrusts along localized shear bands. On the other hand, shallow-layer theory allows the development of simplified results which can predict average mound shapes and identify different scaling regimes for the temporal evolution, without the need for intensive computation.

The scraping of a viscoplastic fluid was investigated by Lister and Hinton [16], who studied the steady-state problem in which fluid entering the mound upstream is balanced by flux under the scraper or around a finite width scraper under the approximations of shallow-layer theory. They calculated the steady-state shape of a quasirigid (yield-stress-dominated) mound in front of both infinite and finite width scrapers, with the latter held perpendicular or obliquely to the direction of travel. They also showed how the steady state is approached for a Newtonian fluid and infinite scraper by assuming that the flux under the scraper is proportional to the free-surface height upstream from the scraper. Maillard *et al.* [6] carried out experiments for the scraping of a layer of Carbopol gel with a thin scraper. They observed an instability resulting in undulations of the free surface upstream of the scraper, and a residual layer of roughly uniform height was left behind the scraper. They also found that the height of the mound was proportional to the square root of its length (after correcting for some initial transient), which they justified theoretically by considering a force balance between the yield stress and hydrostatic pressure, under the assumption that the mound was predominantly unyielded. This assumption was supported by particle image velocimetry measurements that indicated that the mound was approximately rigid, being pushed along by the scraper, and separated from the base by a uniform sheared layer. They did not attempt to compare the experimental free-surface profiles with predictions from shallow-layer (or other) theory.

In this paper, we provide predictions from shallow-layer theory for the shape and time evolution of the free surface of a layer of Bingham or Herschel-Bulkley fluid being scraped from a plane surface by a vertical rigid scraper. We consider the free surface upstream and downstream of the scraper and couple the two regions via the leakage flux through a thin gap under the scraper. In Secs. II–IV, we define the model and provide the governing equations. In Sec. V we compute numerical solutions to the governing equations and provide similarity solutions at early and late times, showing how these predictions are affected by leakage under the scraper, which we model explicitly via a Couette-Poiseuille flow in a narrow rectangular gap under the scraper. In Sec. VI, the predictions for the free-surface profiles are compared against preliminary experiments using a commercial hair gel and show reasonable agreement once a slip boundary condition is included in the model, as motivated by experimental observations of slip. There are also three Appendixes regarding details of the numerical and asymptotic methods.

II. PROBLEM DEFINITION

We analyze the scraping of a layer of viscoplastic fluid, of depth h_∞ from a horizontal plane surface by a scraper traveling at a constant velocity, U, parallel to the surface. We assume a planar flow and that the scraper has infinite width in the out-of-plane direction, so that the motion is purely

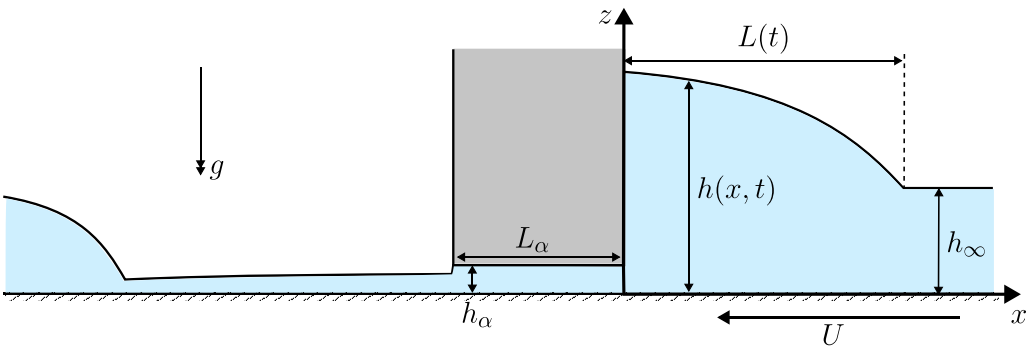

FIG. 1. Schematic of dimensional flow geometry for scraping of a viscoplastic fluid by a scraper of rectangular cross section in the frame of reference moving with the scraper. The free surface is located at $z = h(x, t)$.

two dimensional. Figure 1 shows a schematic of the flow geometry, in the frame of reference moving with the scraper. The free surface, $z = h(x, t)$, has height h_∞ as $x \to \infty$, and the nose of the mound is located at $x = L(t)$; we note that such a position is well defined in the case of a nonzero yield stress, whereas in the absence of a yield stress, the mound upstream of the scraper approaches the far-field height continuously as $x \to \infty$ (see Ref. [16]). L_α and h_α represent the streamwise length of the scraper and the height of the gap under the scraper, which is assumed to be small compared to the far-field fluid height, $h_\alpha \ll h_\infty$. We treat the rheology of the fluid as Herschel-Bulkley, with density, ρ, yield stress, τ_c, consistency K, and shear index, N. The acceleration due to gravity is denoted g.

We work under the lubrication approximation (or "shallow-layer theory"), which requires $h_\infty \ll \mathcal{L}$ where $\mathcal{L}$ is a horizontal length scale for the flow (defined later). Under this approximation, the flow is horizontal to leading order and takes the form of an apparently unyielded plug riding on top of a yielded layer. At higher orders this apparent plug is typically weakly yielded, allowing the plug velocity to vary with x [17]. In the absence of surface tension, following the derivation of Balmforth *et al.* [18] on a horizontal plane and with a change of reference frame to that of the moving scraper, the governing equation is

$$\frac{\partial h}{\partial t} = \frac{\partial}{\partial x}\left\{Uh + \sigma\left(\frac{\rho g}{K}\right)^s \frac{N}{(N+1)(2N+1)}[(2N+1)h - NY]Y^{s+1}\left|\frac{\partial h}{\partial x}\right|^s\right\}, \tag{1}$$

where $\sigma = \mathrm{sgn}(\partial h/\partial x)$, $s = 1/N$, and $Y(x, t)$ is the location of the apparent yield surface,

$$Y = \max\left(0, h - \frac{\tau_c}{\rho g|\frac{\partial h}{\partial x}|}\right). \tag{2}$$

Equation (1) represents the evolution of the free surface height in response to the divergence of horizontal volume flux per unit width. This flux has a contribution due to the translating reference frame [the first term on the right-hand side of (1)], and a contribution from slumping due to gradients of hydrostatic pressure, arising from gradients of free-surface height (the second term on the right-hand side). Where the apparent yield surface vanishes, $Y = 0$, there is no "slumping" since the yield stress is sufficient to support the free surface gradient (in contrast, a Newtonian fluid would exhibit "slumping" or "spreading" unless the free surface is precisely horizontal).

We nondimensionalize vertical lengths by h_∞, velocities by U, horizontal lengths by $\mathcal{L} = \rho g h_\infty^{2+N}/(KU^N)$, a length-scale over which horizontal gradients of hydrostatic pressure balance vertical gradients in viscous shear stresses, and time by $\mathcal{T} = \mathcal{L}/U$. After nondimensionalizing (and relabelling the variables), and noting that $\sigma = -1$ throughout the domain (see Fig. 1 and the results

below), we obtain the governing equation

$$\frac{\partial h}{\partial t} = \frac{\partial}{\partial x}\left\{h - \frac{N[(2N+1)h - NY]}{(N+1)(2N+1)} Y^{s+1} \left|\frac{\partial h}{\partial x}\right|^{s}\right\}, \tag{3}$$

where

$$Y = \max\left(0, h - \frac{\mathrm{Bi}}{|\frac{\partial h}{\partial x}|}\right), \tag{4}$$

and the residual nondimensional parameter in (3) and (4) is the Bingham number,

$$\mathrm{Bi} = \frac{\tau_c}{K(U/h_\infty)^N}, \tag{5}$$

which measures the magnitude of the yield stress relative to viscous stresses developed in the flowing layer. The geometry of the scraper also provides two further dimensionless parameters, $\hat{h}_\alpha = h_\alpha/h_\infty$ and $\hat{L}_\alpha = L_\alpha/\mathcal{L}$. We denote the dimensionless height of the free-surface at the points where it meets the scraper on the up-stream and down-stream side as $h_0(t) = h(0,t)$ and $h_b(t) = h(-\hat{L}_\alpha, t)$, respectively.

Due to the lubrication approximation, we are unable to enforce no-slip or penetration at the scraper. Instead, boundary conditions are obtained by imposing a unit layer thickness in the far field upstream of the scraper and a dimensionless leakage flux at the upstream edge of the scraper, $x = 0$. In the case that there is no gap below the scraper, $h_\alpha = 0$, this outgoing flux is 0; otherwise, there is a leakage flux, Q_α. Lister and Hinton [16] explore the steady state that occurs when this leakage flux approaches unity due to a large jump in hydrostatic pressure between the upstream and downstream sides of the gap. In this case, the residual unyielded layer left behind the scraper is the same height as the incoming layer, and no additional volume is being removed from the layer. The mound of fluid upstream reaches a steady state and is merely advected with the scraper. We will show that this steady state may take a long time to be reached, and, at least at early times, we might instead expect the layer behind the scraper to be approximately uniform and comparable to the gap height h_α (particularly for a high value of the yield stress). This has been observed in experiments. For example, Maillard *et al.* [6] carried out experiments for a similar configuration using Carbopol and observed an approximately uniform residual layer height, given approximately by $1.1h_\alpha$, for the range of conditions they investigated, corresponding to a constant leakage flux. In Sec. III we propose a simple model for the leakage flux as a function of the free-surface height in front and behind the scraper and summarize the full system in Sec. IV. In Sec. V we numerically solve for the full time-dependent evolution of the layer, under this leakage flux model, noting a number of different scaling regimes. Motivated by these solutions, we then explore the evolution of the free surface in the case of a slowly varying leakage flux, for which similarity solutions can be deduced at early and late times, in the cases of viscously or yield-stress-dominated dynamics.

III. LEAKAGE FLUX MODEL

As noted by Lister and Hinton [16], a large mound height at the scraper results in a high hydrostatic pressure at the gap between the scraper and surface, which may drive additional leakage flux through this gap. One model for the leakage flux when the gap is small, i.e., $h_\alpha \ll L_\alpha$ (see Fig. 1), is to assume a Couette-Poiseuille flow in the gap. Assuming hydrostatic pressure ahead of and behind the scraper, the dimensionless horizontal pressure gradient in the thin gap is given approximately by

$$\frac{\partial p}{\partial x} = G = \frac{h_0 - h_b}{\hat{L}_\alpha}. \tag{6}$$

As discussed in Appendix A, it is convenient to define a gap-scaled pressure gradient and Bingham number by $P = G\hat{h}_\alpha^{N+1}$ and $\mathrm{Bi}_g = \mathrm{Bi}\hat{h}_\alpha^N$, respectively, and report the dimensionless flux under the

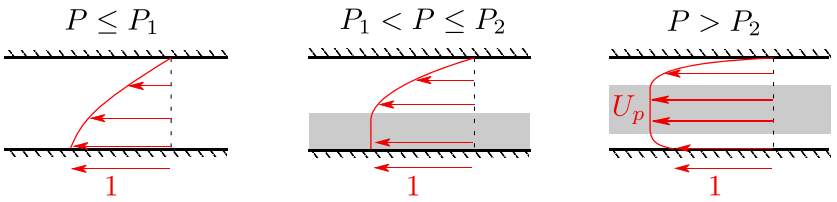

FIG. 2. Schematic of the nondimensional velocity profiles in the gap under the scraper for the three different regimes of the scaled nondimensional pressure gradient, $P = G\hat{h}_\alpha^{N+1}$. Unyielded plug regions are shaded gray.

scraper (in the negative x direction), Q_α, as a function of P and Bi_g. The algebraic expressions for the flux can be found in Appendix A and their derivation can be found in Ref. [19, Chapter 7] and, in a slightly different form, in Ref. [20]. Below we give an overview of the physical context behind the algebraic results provided in the Appendix.

The complication in deriving the leakage solution lies in the existence of three distinct regimes under the scraper, depending on the gap-scaled pressure gradient, P. Figure 2 illustrates these three regimes. First, for sufficiently small pressure gradients, the flow under the scraper is dominated by the shear arising from the translating boundary and the fluid is yielded throughout the gap. Increasing the pressure gradient increases the curvature of the velocity profile in the gap and hence increases the flux. At a critical value, $P = P_1$ (given in Appendix A), the shear rate vanishes at the bottom boundary and, at larger pressure gradients, this results in an unyielded plug that translates with the bottom boundary. It is perhaps unintuitive that increasing the driving pressure gradient can result in the formation of an unyielded plug. This occurs because the increased driving pressure gradient results in a faster flow of fluid through the gap, so that the translating lower boundary is no longer the primary driver of the flow. In particular, the driving stress exerted by this boundary decreases and eventually becomes lower than the yield stress of the fluid. As the pressure gradient increases further, the stress exerted by the boundary switches from being a driving stress in the flow direction to a resistive stress opposing the flow, because the pressure gradient would otherwise act to drive a flow that exceeds the velocity of the bottom boundary. Initially, no change occurs to the structure of the solution until a second critical pressure gradient, $P = P_2$, is reached, at which the resistive stress of the lower boundary exceeds the yield stress and the fluid becomes yielded in a region between the plug and the bottom boundary. The plug is then detached from both boundaries and travels at a velocity, U_p, which exceeds the unit velocity (in dimensionless units) of the boundary. As the pressure gradient is then increased further, leakage flux increases as a result of this plug velocity increasing.

Two simplified regimes for the leakage flux can be deduced. First, when the pressure gradient is small, $P \ll 1$, the velocity profile in the gap is approximately linear, and the flux is given to leading order by

$$Q_\alpha = \frac{\hat{h}_\alpha}{2}, \tag{7}$$

which is also obtained from the small P regime of the full flux expression [(A3) and (A4)]. Second, in the final regime, $P > P_2$, the leakage flux can become arbitrarily large with increasing P (via arbitrarily large plug velocities). Thus, for some P the leakage flux becomes equal to 1 and the scraper system reaches a steady state since the flux under the scraper matches the incoming flux from the far field, as envisaged by Lister and Hinton [16]. Since the average velocity in the gap is at most the plug velocity, this requires $U_p = O(1/\hat{h}_\alpha) \gg 1$, when the gap is small, $\hat{h}_\alpha \ll 1$. This, in turn, requires a large pressure gradient $P \gg 1$. Expansion of the flux given in the Appendixes [(A9)–

(A11)], for large P, then gives

$$\frac{Q_\alpha}{\hat{h}_\alpha} = \frac{P^s}{2^{s+1}(s+2)}\left(1 - \frac{2\mathrm{Bi}_g}{P}\right)^{s+1}\left[1 + \frac{2\mathrm{Bi}_g}{(s+1)P}\right], \tag{8}$$

to leading order. Since $Q_\alpha = O(1)$ in this regime, provided $\mathrm{Bi}_g \ll \hat{h}_\alpha^{-N}$ [for example when $\mathrm{Bi} = O(1)$] we find that $P = O(\hat{h}_\alpha^{-N})$, and (8) reduces to

$$\frac{Q_\alpha}{\hat{h}_\alpha} = \frac{P^s}{2^{s+1}(s+2)} + \ldots, \tag{9}$$

which corresponds to the relationship between flux and pressure gradient for a standard plane-Poiseuille flow of a power-law fluid.

The scaled pressure gradient at steady state can then be found implicitly by setting $Q_\alpha = 1$ in (8) [or its approximation (9)]. In this regime, the upstream height of the fluid is much larger than the downstream height, $h_0 \gg h_b$, and thus the pressure gradient is given to leading order by $G = h_0/\hat{L}_\alpha$. The steady-state height of the mound at the upstream edge of the scraper, denoted H_0, is then determined to leading order from $H_0 = P\hat{h}_\alpha^{-(N+1)}\hat{L}_\alpha$. In particular, under the assumption that $\mathrm{Bi} \ll O(\hat{h}_\alpha^{-2N})$, we find

$$H_0 = 2^{N+1}(s+2)^N \hat{L}_\alpha \hat{h}_\alpha^{-(2N+1)} + \ldots. \tag{10}$$

Note that, at this stage, it is not clear whether the steady state is reached in finite time or approached asymptotically; this is determined later, in Sec. V B, where we show that the difference from the steady state decays exponentially in time.

Figures 3(a)–3(c) shows plots of Q_α against G for a Bingham fluid ($N = 1$) with $\hat{h}_\alpha = 0.1$ and three different values of Bi [see (A12)]. These show how, since $\hat{h}_\alpha$ is small, the gradient $dQ_\alpha/dG = \hat{h}_\alpha^{N+1} dQ_\alpha/dP = O(\hat{h}_\alpha^{N+2})$, is very small, requiring significant variation in G (and hence h_0) to lead to variation in Q_α. Similarly, Figs. 3(d)–3(f) shows the leakage flux calculated by this model for a Herschel-Bulkley fluid of shear index $N = 0.5$ at the same values of Bi. Compared with the Bingham case, for moderate Bingham numbers the steady state, $Q_\alpha = 1$, is reached for significantly lower (though still relatively large) dimensionless pressure gradients, G. This is to be expected since the high shear rate in the thin gap under the scraper results in a lower effective viscosity for the fluid and, thus, a greater leakage flux for the same imposed pressure gradient.

Another notable feature is that, in the regime of a large Bingham number, there is a wide range of G over which the leakage flux varies even more slowly [this can be deduced from (A6) and seen in Figs. 3(c) and 3(f)]. This is because the difference between the two critical pressure gradients, P_1 and P_2, is $O(\mathrm{Bi}_g)$ which implies the second regime occurs over an $O(\mathrm{Bi}/\hat{h}_\alpha)$ range of G when $\mathrm{Bi} \gg 1$. Throughout much of this regime, the dimensionless leakage flux is approximately given by the gap size, $Q_\alpha \approx \hat{h}_\alpha$ [see (A6)], which can be understood as the sheared region between the unyielded plug and the underside of the scraper (see Fig. 2) becoming a thin boundary layer when $\mathrm{Bi} \gg 1$, and hence the flow under the scraper being given to leading order by a plug flow of height $\hat{h}_\alpha$ and unit velocity (for which the leakage flux is $\hat{h}_\alpha$). This is consistent with the intuition that, for a large yield-stress fluid, such a scraper would typically "cut" the fluid down to a layer of height dictated by the gap height.

Regardless of the magnitude of Bi, the steady state requires a large pressure gradient to be reached and consequently only occurs after a sufficiently high mound [$h_0 \geqslant O(10^4)$ for $N = 1$ and $\hat{h}_\alpha = 0.1$] has built up in front of the scraper. Given the slow variation in Q_α, an appropriate simplification which is valid at early times, is to take the leakage flux as constant to leading order. Over very large timescales, however, the varying flux becomes relevant, which in particular allows for a steady state ultimately to be approached. In Sec. V, numerical simulations and similarity solutions are used to explore the evolution of the free surface in different regimes. First we summarize the full system in Sec. IV.

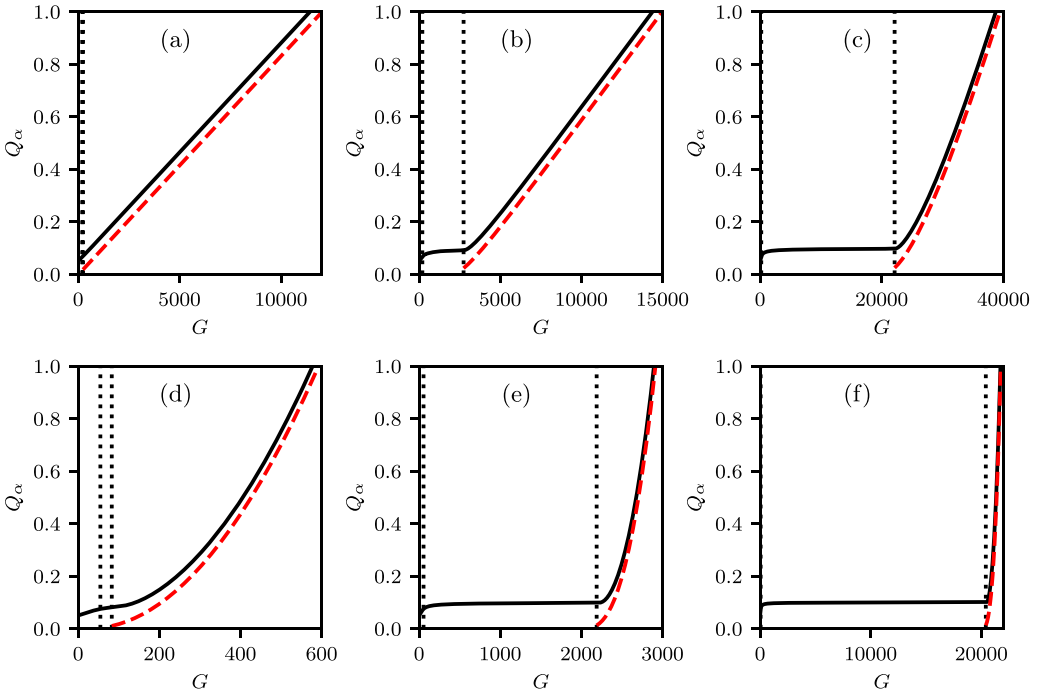

FIG. 3. Dimensionless leakage flux, Q_α, as a function of the dimensionless pressure gradient under the scraper, G, for [(a)–(c)] a Bingham fluid ($N = 1$) and [(d)–(f)] a Herschel-Bulkley fluid with $N = 0.5$. The additional dimensionless parameters are $\hat{h}_\alpha = 0.1$ and [(a) and (d)] Bi $= 1$, [(b) and (e)] Bi $= 100$, and [(c) and (f)] Bi $= 1000$. The transitions between different flow regimes under the scraper are marked by vertical dotted lines (the two transitions are essentially indistinguishable in the first panel), and the approximation for large G [Eq. (8)] are shown as red dashed lines.

IV. THE FULL SYSTEM OF GOVERNING EQUATIONS

To summarize, given an initial free-surface profile $h(x, 0)$, the Bingham number, Bi, shear index, N, and the nondimensional height, $\hat{h}_\alpha$, and length, $\hat{L}_\alpha$, of the gap under the scraper, we compute the nondimensional elevation of the free surface, $h(x, t)$, and the yield-surface height, $Y(x, t)$, for times $t > 0$, in front ($x > 0$) and behind ($x < -\hat{L}_\alpha$) the scraper. The yield surface height at any given moment is determined directly from the free-surface profile, via (4), and the evolution of h is governed by (3), with boundary conditions,

$$h = 1 \quad \text{for } x \to \pm\infty. \tag{11}$$

The evolution in the two domains ($x > 0$ and $x < -\hat{L}_\alpha$) are coupled via the flow under the scraper, which enforces

$$h - \frac{N[(2N+1)h - NY]}{(N+1)(2N+1)} Y^{s+1} \left|\frac{\partial h}{\partial x}\right|^s = Q_\alpha \tag{12}$$

at the edges of the scraper: $x = -\hat{L}_\alpha$ and $x = 0$. Here Q_α depends on h_0 and h_b and is evaluated as detailed in Sec. III and Appendix A.

As discussed in Sec. III, if we assume $\hat{h}_\alpha \ll 1$ and $\hat{L}_\alpha = O(1)$, then at early times (when h_0, $h_b \approx 1$) we lie in the first regime of the leakage flux and the constant term, $Q_\alpha \approx \hat{h}_\alpha/2$, dominates its value. Thus we can assume an initially constant leakage flux of magnitude $\hat{h}_\alpha/2$ to provide an initial free-surface profile via an early-time similarity solution detailed later in Sec. V A. We then integrate

numerically from this initial condition, using the method described in Appendix B, with leakage flux given by (A3)–(A11). In this numerical integration, the treatment of the region downstream of the scraper requires some care. As discussed in Appendix B, behind the scraper the free surface first decreases with time before reaching a singular point where $h_b = Q_\alpha$. After this point, provided the leakage flux does not vary sufficiently rapidly for the layer to become yielded again, (12) implies that the scraper simply leaves an unyielded residual layer behind it, such that $h_b = Q_\alpha$ at the back of the scraper at all times. This layer is advected to the left with unit velocity, and so, within this unyielded layer, we have $h(x,t) = Q_\alpha(t-x)$. As discussed in Sec. III, Q_α varies very slowly, and thus the gradient of the free-surface height, $\partial h/\partial x$, will be small in this region—supporting the assumption that the layer does not ever become yielded again. Furthermore, since the rate of increase of the free surface height in front of the scraper, h_0, decreases with time, the rate of increase of Q_α, and the slope of the free surface behind the scraper decrease with time, further preventing additional yielding in the layer.

V. MODEL RESULTS AND SCALING REGIMES

Figure 4 shows results of a numerical simulation with parameters $N = 1$, $\hat{h}_\alpha = 0.2$, $\hat{L}_\alpha = 0.5$, and $\mathrm{Bi} = 5$. The first three panels show the dimensionless free surface layer height, $h(x)$, which demonstrates: the initial development of the mound upstream and depression downstream of the scraper at early times [Fig. 4(a)], the stage in which the residual layer immediately behind the scraper is unyielded and we have $h_b = Q_\alpha$ [Fig. 4(b)], and the increase of the leakage flux to $Q_\alpha = 1$ over a very large timescale and the resulting steady-state mound upstream of the scraper [Fig. 4(c)]. In this third panel, the vertical scale is logarithmic and the horizontal scale is piecewise linear but differs between the upstream and downstream regions, so that both can be viewed on the same plot.

Figures 4(d)–4(f) show the height, h_0, length, L, of the mound, and the leakage flux, Q_α, as functions of time, from the same numerical solution as shown in Figs. 4(a)–4(c). Further time series for the free surface height, h_0, from different numerical solutions are shown in Fig. 5 (for Bingham fluids, $N = 1$) and Fig. 6 (for shear-thinning fluids with $N = 0.5$). These results demonstrate the key characteristics of solutions with small $\hat{h}_\alpha$. Namely a very large dimensionless time is required before steady state is reached, and a number of different power-law regimes are observed as the flow evolves to the steady state. In particular, all results indicate an early-time regime in which the height and length scale like $t^{1/2}$, before a transition to an intermediate regime (i.e., $t \gg 1$ but before the steady state is reached) in which a number of different power laws are possible. We will rationalize the early time behavior via a constant leakage flux similarity solution, while the approach to steady state ($Q_\alpha \sim 1$) and intermediate times (namely $t \gg 1$ with $Q_\alpha \ll 1$) can be understood by assuming a quasisteady shape of the mound upstream of the scraper, similarly to the analysis by Lister and Hinton [16] for the purely viscous problem.

In particular, we will show that three cases are possible in the evolution to the steady state. These three cases are demonstrated in Fig. 5. In all cases there is an early-time solution for which the height and length of the mound scale as $t^{1/2}$. This regime transitions into a quasistatic regime for $t \gg 1$. The "intermediate," quasistatic regime may be yield-stress dominated throughout and transition to the steady state after a yield-stress-dominated timescale, T_y [Fig. 5(a)]. Alternatively, it can be viscously dominated throughout, transitioning to the steady state after a viscously dominated timescale, T_v [Fig. 5(c)]. Finally, the intermediate regime can start off as viscously dominated, before transitioning to a yield-stress-dominated regime on a transition timescale, T_t [Fig. 5(b)]. The steady state is then again reached on the yield-stress-dominated timescale, T_y. We detail these regimes and timescales, primarily focusing on the case of a Bingham fluid ($N = 1$) for clarity of exposition, in the following sections. In Sec. V C we then briefly discuss the analogous timescales for $N \neq 1$.

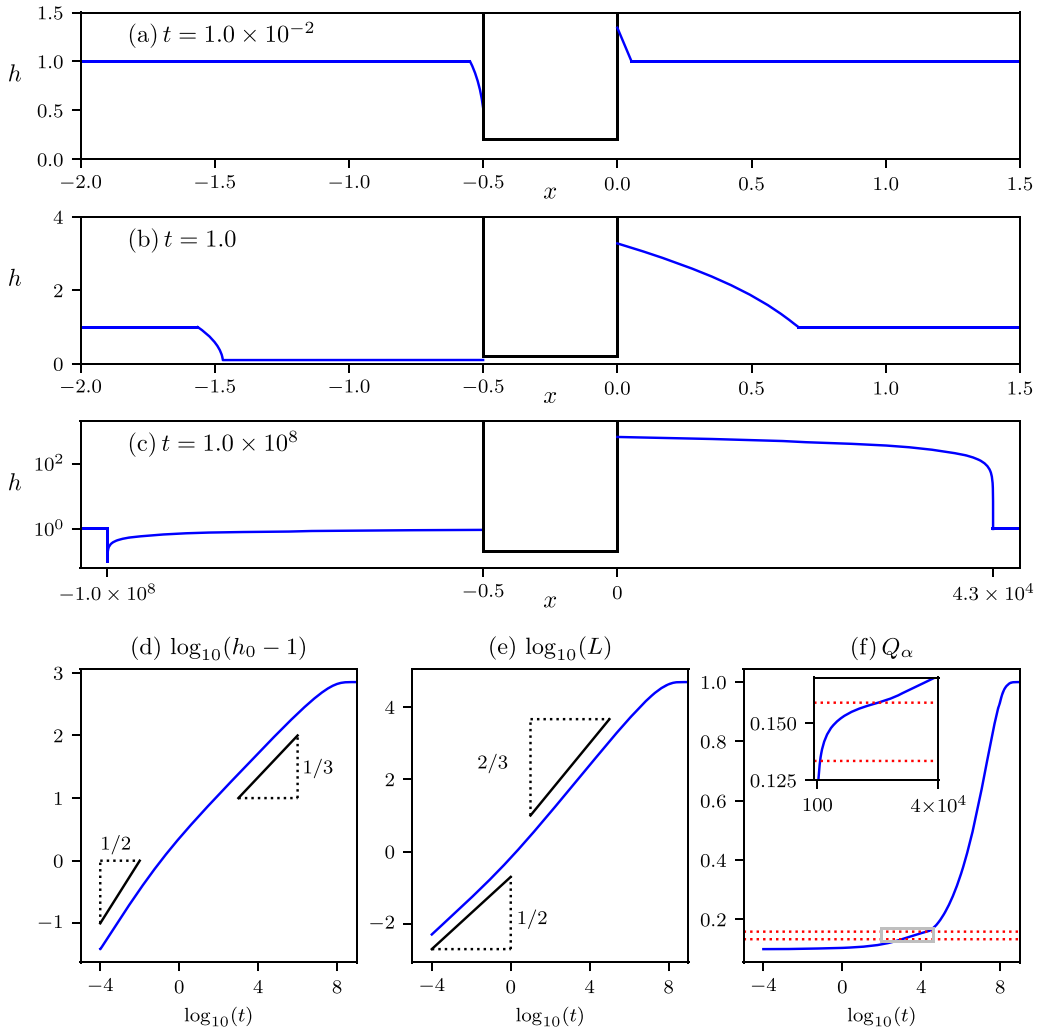

FIG. 4. Results of a numerical solution for the model summarized in Sec. IV with Bi = 5, $N = 1$, $\hat{h}_\alpha = 0.2$, and $\hat{L}_\alpha = 0.5$. [(a)–(c)] Profiles of layer height, $h(x)$, at $t = 0.01$, 1, and 10^8, with the outline of the scraper shown in black. Panels (a) and (b) use a uniform linear scale, while panel (c) uses a logarithmic scale for the vertical axis and a nonuniform linear scale for the horizontal axis. Here the different scales upstream and downstream of the scraper are indicated on the axis, and the scale is linear between the indicated points. [(d)–(f)] Time series of the numerical solution: (d) Difference between the free-surface height at the scraper and in the far field, $h_0 - 1$, on a log-log scale; (e) length of the disturbance upstream of the scraper, L, on a log-log scale; and (f) the leakage flux, Q_α, on a semilog scale with detail on a linear scale (inset). Dotted red lines show the transition between the different regimes discussed in Sec. III.

A. Early time

As established in Sec. III, when $\hat{h}_\alpha \ll 1$ and at early times during the evolution, the leakage flux is constant to leading order, given by $Q_\alpha = \hat{h}_\alpha/2 \ll 1$. We can then find a leading-order similarity solution for the early time evolution of the mound in the region upstream of the scraper ($x > 0$) assuming this constant leakage flux. We seek solutions of the form

$$h = 1 + t^b \mathcal{H}(\xi), \quad Y = t^c \mathcal{Y}(\xi), \tag{13}$$

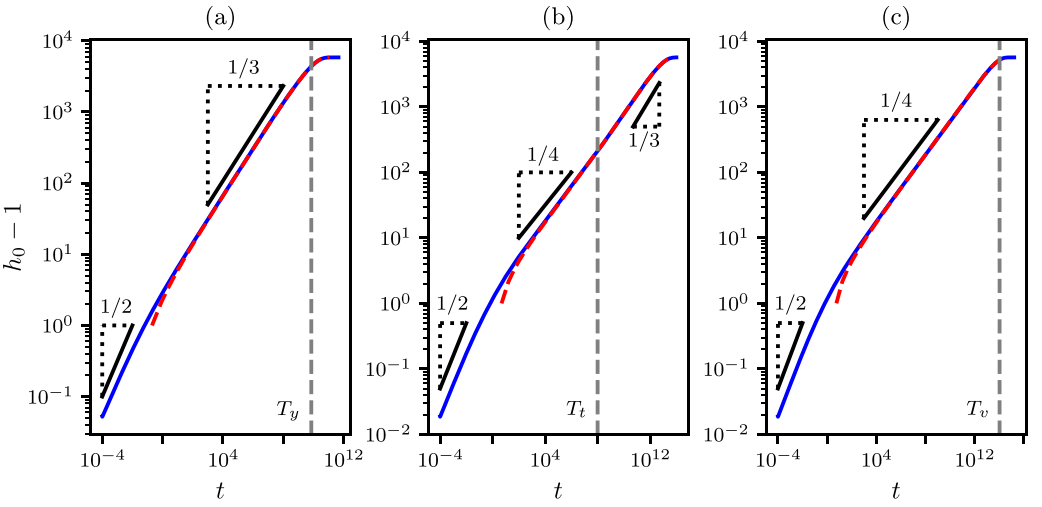

FIG. 5. Numerical solutions (solid blue) for dimensionless maximum free-surface height, h_0, as a function of time, t, on a log-log scale. Parameters are $\hat{h}_\alpha = 0.1$, $\hat{L}_\alpha = 0.5$, and (a) Bi $= 10$, (b) Bi $= 0.01$, and (c) Bi $= 0.001$. The red dashed line shows the quasistatic prediction given by (26), and the gray dashed lines give the predicted timescales for the approach to steady state in the yield-stress-dominated regime, T_y (a), the transition between viscously and yield-stress-dominated behavior, T_t (b), and the approach to steady state in the viscously dominated regime, T_v (c).

where

$$\xi \equiv \frac{x}{L(t)} = \frac{x}{x_N t^a}, \tag{14}$$

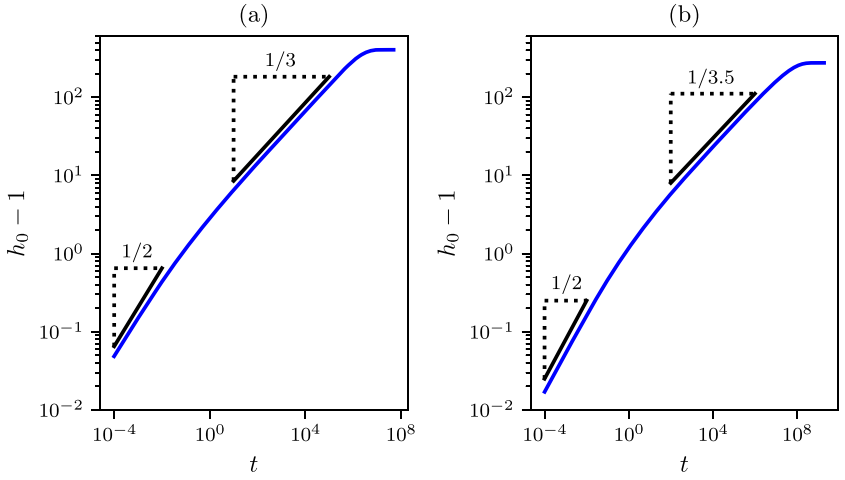

FIG. 6. Numerical solutions (solid blue) for dimensionless maximum free-surface height, h_0, as a function of time, t, on a log-log scale for a Herschel-Bulkley fluid. Parameters are $\hat{h}_\alpha = 0.1$, $\hat{L}_\alpha = 0.5$, $N = 0.5$, and (a) Bi $= 10$ and (b) Bi $= 0.001$. The slope indicators show the predicted scalings at early times, $t \ll 1$, and intermediate times, $t \gg 1$ with $Q_\alpha \ll 1$, for the yield-stress and viscously dominated behaviors [in (a) and (b), respectively].

$L(t) = x_N t^a$ is the length of the deformed region, $0 \leqslant \xi \leqslant 1$, and a, b, and c are all non-negative. The boundary conditions at the nose of the mound are given by

$$\mathcal{H}(1) = \mathcal{Y}(1) = 0, \tag{15}$$

which represent the conditions that the fluid is unyielded and of height 1 at the nose. Note that unit flux at the nose, where the deformed free surface meets the incoming unyielded layer, is automatically satisfied by (15), and that the flux condition at the scraper (12) can be replaced by a global mass conservation condition,

$$t^{a+b} x_N \int_0^1 \mathcal{H} d\xi = (1 - Q_\alpha) t, \tag{16}$$

which gives $a + b = 1$ and $\int_0^1 \mathcal{H} d\xi = (1 - Q_\alpha)/x_N$.

On substitution of (13) and (14) into the governing equations (3) and (4), we find that the divergence of the flux is dominated by variations in the free-surface gradient (i.e., "slumping"), and we can neglect the advective term in (3) due to variations in the free-surface height. We thus find that $b - 1 = (s + 1)c + sb - (s + 1)a$ [i.e., $(s + 1)c = 2sa - s$]. Then, for balance in the yield equation (4), we find $a - b = c = 0$ and so $a = b = 1/2$. Thus we obtain the early-time timescale, $h_0 - 1 \sim t^{1/2}$, $L \sim t^{1/2}$, as is observed in all numerical solutions shown in Figs. 4–6. We note that this scaling is independent of the shear index N.

The similarity solution can further be used to obtain the shape of the free-surface profile at early times. We focus on the case of a Bingham fluid ($N = 1$) in the following analysis, although the case of a Herschel-Bulkley fluid could be considered analogously. On substituting the rescaled similarity variable, $\mathcal{H} = x_N \mathrm{Bi} \hat{H}$, and setting $N = 1$, the governing equations reduce to the ordinary differential equation (ODE),

$$\hat{H} - \xi \hat{H}' = \frac{1}{3x_N^2} [\mathcal{Y}^2 (3 - \mathcal{Y}) \hat{H}']', \qquad \text{where} \qquad \mathcal{Y} = 1 + \frac{1}{\hat{H}'}, \tag{17}$$

and a prime denotes differentiation with respect to ξ. The boundary conditions are

$$\hat{H}(1) = \mathcal{Y}(1) = 0 \qquad \text{and} \qquad x_N^2 \int_0^1 \hat{H} \, d\xi = \frac{1 - Q_\alpha}{\mathrm{Bi}}. \tag{18}$$

This system (17) and (18) can be numerically integrated to determine the similarity profiles, $\hat{H}$ and $\mathcal{Y}$, as well as the front position, x_N. The numerical method is described in detail in Appendix C. For a given value of x_N, (17) is integrated from $\xi = 1$ to $\xi = 0$ and then (18 c) provides the corresponding values of $\mathrm{Bi}/(1 - Q_\alpha)$. In other words, the front position, x_N, is a function of only the ratio $\mathrm{Bi}/(1 - Q_\alpha)$.

In Fig. 7 we plot the variation of x_N and $\hat{H}(0)$ as a function of the ratio $\mathrm{Bi}/(1 - Q_\alpha)$. It is particularly insightful to consider the behavior when $\mathrm{Bi} \gg (1 - Q_\alpha)$. In this yield-stress-dominated regime, $x_N = O\{[\mathrm{Bi}/(1 - Q_\alpha)]^{-1/2}\}$, while $\hat{H}$ remains of order unity. For balance in (17 a), we then require $\mathcal{Y} = O\{[\mathrm{Bi}/(1 - Q_\alpha)]^{-1/2}\} \ll 1$, which implies that the mound upstream of the scraper is unyielded to leading order, and the governing equation (17 b) is satisfied by requiring that $\mathcal{Y} = 0$. Thus

$$1 + \frac{1}{\hat{H}'} = 0, \tag{19}$$

which has solution

$$\hat{H} = 1 - \xi \qquad \text{and} \qquad x_N = \sqrt{\frac{2(1 - Q_\alpha)}{\mathrm{Bi}}}. \tag{20}$$

This yield-stress-dominated solution gives a triangular free surface height with $O(\mathrm{Bi})$ slope in the unscaled variables. In Fig. 7(a), the results for $\hat{H}(0)$ and x_N are scaled by the predictions of this

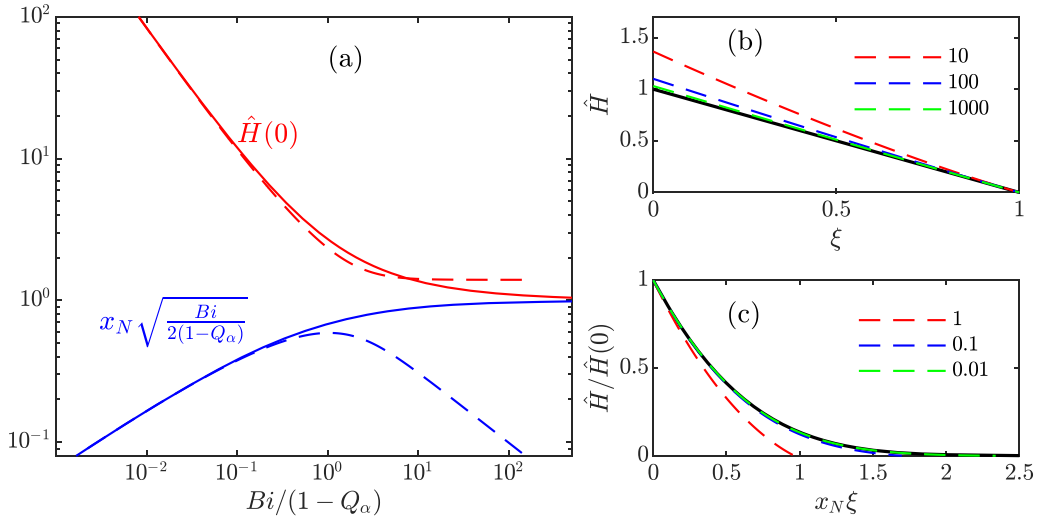

FIG. 7. (a) Height, $\hat{H}(0)$ (red), and length [scaled by the yield-stress-dominated result (20)], $x_N\sqrt{\mathrm{Bi}/2(1-Q_\alpha)}$ (blue), for the early time similarity solution, as functions of the ratio $\mathrm{Bi}/(1-Q_\alpha)$. The dashed lines show the asymptotic predictions in the viscously dominated regime, $\mathrm{Bi} \ll 1-Q_\alpha$. (b) Height profiles from the early time similarity solution at three values of $\mathrm{Bi}/(1-Q_\alpha)$ (as shown in legend) compared against the yield-stress-dominated asymptotic solution, (20) (black). (c) Scaled height, $\hat{H}/\hat{H}(0)$, plotted against scaled similarity coordinate, $x_N\xi$, for three values of $\mathrm{Bi}/(1-Q_\alpha)$ (as shown in legend), compared against the outer solution in the viscously dominated asymptotic solution, detailed in Appendix C (black).

asymptotic solution, and thus these curves asymptote to 1 as the ratio $\mathrm{Bi}/(1-Q_\alpha)$ becomes large. The asymptotic prediction for the free surface profile, is also compared with the solution of (17) and (18) for the cases of $\mathrm{Bi}/(1-Q_\alpha) = 10$, 100, and 1000 in Fig. 7(b), evidencing the convergence to the asymptotic solution.

It is also possible to deduce the asymptotic solution in the regime where $\mathrm{Bi}/(1-Q_\alpha)$ is small. This corresponds to a weak yield stress and the solution is close to the viscous solution [9], modified only when the front is approached. It is nevertheless possible to deduce leading-order expressions for x_N and $\hat{H}(0)$ using a matched asymptotic argument that is presented in Appendix C, and which are plotted with dashed lines in Fig. 7(a). In general, the mound becomes of lower aspect ratio and increased convexity in this regime. Again, the asymptotic solution is compared with the solution of (17) and (18) for the cases of $\mathrm{Bi}/(1-Q_\alpha) = 1$, 0.1, and 0.01, evidencing the convergence to the asymptotic solution [see Fig. 7(c)], which is remarkably good, even at the modest value of 0.1.

Early time solutions were also calculated numerically from the full equations (3) and (4). The numerical method described in Appendix B was used to integrate from $t = 0$ to $t = 10^{-2}$, and the results compared with the similarity solutions (see Fig. 8), showing close agreement which diverges with increasing time, as anticipated. The similarity solution was derived on the basis that the divergence of the flux was dominated by variations in the free-surface gradient (i.e., "slumping"), neglecting the advective term in the equation due to variations in the free-surface height. This required that $|\partial(Y^2\partial h/\partial x)/\partial x| \gg |\partial h/\partial x|$ which implies $x/Y^2 \ll 1$. Thus, when $\mathrm{Bi}/(1-Q_\alpha) \leqslant O(1)$, we have $Y = O(1)$ and $x \sim t^{1/2}$, and so the similarity solution becomes invalid once t becomes order unity, when the horizontal length scale of the mound is no longer small compared to the typical length scale of the problem, $\mathcal{L}$. When the yield stress dominates, $\mathrm{Bi}/(1-Q_\alpha) \gg 1$, the similarity solution becomes invalid at earlier times, since the yield stress inhibits slumping. Specifically, when $\mathrm{Bi}/(1-Q_\alpha) \gg 1$ we have shown that $x \sim x_N\, t^{1/2} \sim [t(1-Q_\alpha)/\mathrm{Bi}]^{1/2}$ and $Y \sim \mathcal{Y} \sim [\mathrm{Bi}/(1-Q_\alpha)]^{-1/2}$. Hence, the advection term can be neglected in comparison to the slumping term when $x/Y^2 \sim [t\mathrm{Bi}/(1-Q_\alpha)]^{1/2} \ll 1$. Thus, in this regime we anticipate the similarity solution

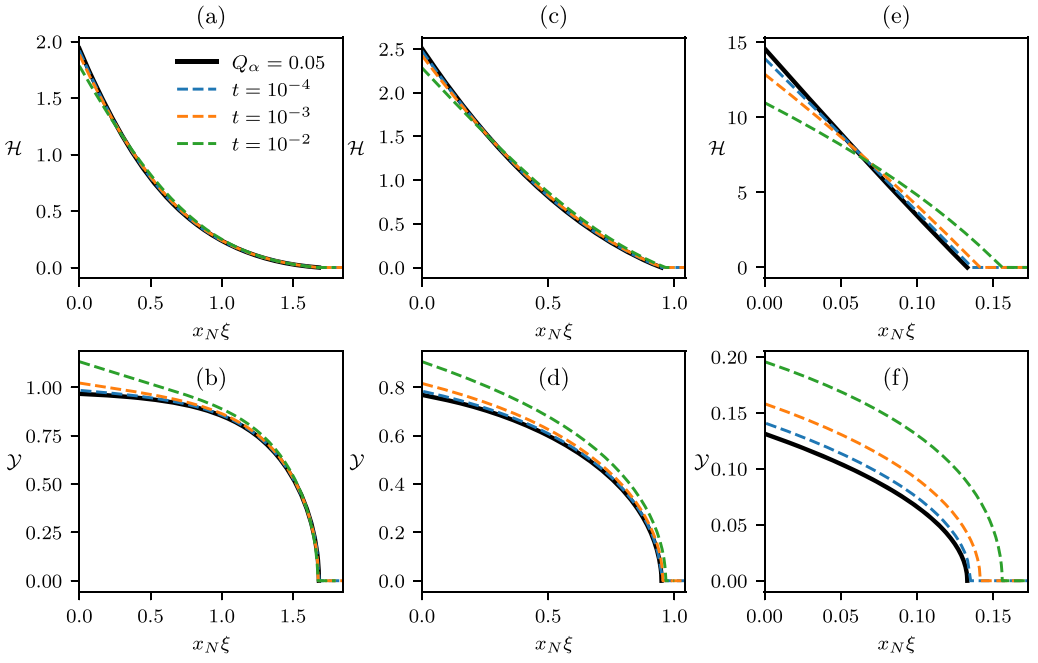

FIG. 8. Early time similarity solutions (black solid lines) for the free-surface height (top row) and yield-surface height (bottom row) compared with numerical solutions at $t = 10^{-4}$, 10^{-3}, and 10^{-2} (dashed lines, see legend) for $Q_\alpha = 0.05$, and Bi = 0.1, 5, and 100 [(a) and (b), (c) and (d), and (e) and (f), respectively]. Solutions are scaled according to the similarity solution derived in Sec. V A.

to become invalid when $t = O[(1 - Q_\alpha)/\mathrm{Bi}]$. This is evidenced in Figs. 8(e) and 8(f), where the discrepancy between the numerical and asymptotic solutions is already significant at $t = 10^{-2}$.

If the fluid layer initially also has $h = 1$ behind the scraper, then the early time deformation behind the scraper is a reflection of the free surface in front of the scraper. In particular, if we define

$$\hat{H}_b(\xi) = -\hat{H}(-\xi), \quad \mathcal{Y}_b(\xi) = \mathcal{Y}(-\xi), \tag{21}$$

then $\hat{H}_b$ and $\mathcal{Y}_b$ satisfy (17) in the region $-1 \leqslant \xi \leqslant 0$, representing the deformed region behind the scraper, and $\hat{H}_b$ satisfies

$$x_N^2 \int_{-1}^{0} \hat{H}_b d\xi = -\frac{(1 - Q_\alpha)}{\mathrm{Bi}}, \tag{22}$$

as required behind the scraper by mass conservation.

B. Intermediate-time and approach to steady state

At later times, the dominant balance in the governing equation changes and the unsteady term is negligible to leading order. The solution upstream of the scraper therefore evolves through a series of quasistatic states in which the volume flux is unity to match the flux far upstream. Again focusing on the case of a Bingham fluid ($N = 1$), we neglect the time derivative in (3) and (4) and integrate once to obtain

$$\frac{1}{6}Y^2(3h - Y)\frac{\partial h}{\partial x} + h = 1, \quad \text{and} \quad Y = h + \frac{\mathrm{Bi}}{\partial h/\partial x}. \tag{23}$$

We can then find the volume of the mound, V, as a function of the free-surface height at the scraper, h_0, by numerical integration of (23a) and 23(b) from the nose of the mound, where $h = 1$ and $Y = 0$, up until reaching $h = h_0$, where we evaluate the volume $V(h_0)$.

Additionally, at late times the height of the free surface at the upstream face of the scraper satisfies $h_0 \gg 1$, while downstream we have $h_b \leqslant 1$. Hence, the hydrostatic pressure gradient under the scraper, and by implication the leakage flux, is dominated by the variation in the upstream free-surface height, h_0. Hence, we can approximate the leakage flux (A12) by

$$Q_\alpha = Q_\alpha[G = (h_0 - h_b)/\hat{L}_\alpha)] \approx Q_\alpha(h_0/\hat{L}_\alpha), \tag{24}$$

which can be interpreted as a function only of h_0, since $\hat{L}_\alpha$ is a fixed parameter of the problem.

This leads to an ODE for h_0, by noting that

$$\frac{d}{dt}V(h_0) = V'(h_0)\frac{dh_0}{dt} = 1 - Q_\alpha, \tag{25}$$

where $'$ represents differentiation with respect to h_0. Integrating the approximation (25) gives (cf. Ref. [16])

$$t(h_0) = \int_1^{h_0} \frac{V'(h)}{1 - Q_\alpha} dh = \frac{V(h_0)}{1 - Q_\alpha} - \int_1^{h_0} \frac{V(h)}{(1 - Q_\alpha)^2}\frac{dQ_\alpha}{dh_0} dh, \tag{26}$$

where integration by parts is used to express the integral in terms of dQ_α/dh_0, which can be derived analytically from (A12). This gives an implicit relation for the free-surface height, h_0, as a function of t. In deriving this relation two approximations were made, namely that the mound is quasistatic and that the leakage flux is independent of the height behind the scraper. Both of these approximations require large time, $t \gg 1$, for which we assume the height and the length of the mound are both large, $h, L \gg 1$. Along with the volume constraint, $hL \sim t$, this implies $h \sim t/L \ll t$ and $L \sim t/h \ll t$. The quasistatic assumption requires that the dimensionless adjustment timescale, t, is much larger than the advection timescale, which is given by the time taken for the bottom boundary to travel the length of the mound, L. Thus, this approximation applies when $t \gg L$, which we have shown is true for $t \gg 1$. The use of 1 as the lower limit of the integration in (26) implies the use of the quasistatic assumption throughout the history of the evolution of the mound, including early times at which the assumption does not apply. As such, there is a constant of integration missing from (26) which would account for the initial stages of the evolution of the mound; however, this constant is asymptotically small at large times and can be neglected to leading order.

During this regime, the quasistatic solution can be yield-stress- or viscously dominated, depending on which terms balance in (23b). The solution will be yield-stress dominated if the balance is between the two terms on the right-hand side of (23b), which requires $h^2/L \sim \mathrm{Bi}$. The viscously dominated regime thus occurs if $h^2/L \gg \mathrm{Bi}$, in which case the balance in (23b) is $Y \sim h$. A consequence is that there can only ever be a transition from the viscously dominated regime to the yield-stress-dominated regime, because, as will be shown, in the viscously dominated regime, h^2 grows slower than L, while in the yield-stress-dominated regime, these quanitities scale in the same way (via $h^2/L \sim \mathrm{Bi}$).

We now derive the leading-order solutions in the yield-stress- and viscously dominated regimes and identify the timescales on which the steady state is reached (T_y or T_v, respectively) and on which a transition between the regimes can occur (T_t).

1. Yield-stress-dominated quasistatic regime

In the yield-stress-dominated regime we have $Y \ll h$ and the leading order of (23b) gives

$$h + \frac{\mathrm{Bi}}{\partial h/\partial x} = 0 \Rightarrow h = \sqrt{2\mathrm{Bi}(L - x)}, \tag{27}$$

and

$$V(h_0) = \frac{h_0^3}{3\mathrm{Bi}}. \tag{28}$$

The leading order of (23a) gives

$$\frac{1}{2}Y^2 h\frac{\partial h}{\partial x} + h = 0, \tag{29}$$

and we obtain the height of the yield surface,

$$Y = \left[\frac{8}{\mathrm{Bi}}(L-x)\right]^{1/4}. \tag{30}$$

When $Q_\alpha \ll 1$ and $dQ_\alpha/dh_0 \ll 1$, which is applicable for intermediate times when $\hat{h}_\alpha \ll 1$ (see Sec. III), we can evaluate (26) to obtain

$$h_0 = (3\mathrm{Bi}\,t)^{1/3} + \ldots, \quad L = \frac{h_0^2}{2\mathrm{Bi}} + \ldots = \frac{3^{2/3}}{2\mathrm{Bi}^{1/3}}t^{2/3} + \ldots, \tag{31}$$

giving a $1/3$ power law for h_0 and a $2/3$ power law for L as a function of t, as observed in the numerical solution shown in Fig. 4. This solution, (27)–(31), is equivalent to the solution for a quasistatic mound of viscoplastic fluid extruded at a constant rate from a line source [21]. The shape of the free surface further corresponds to the quasirigid bow wave constructed by Lister and Hinton [16] and previously reported in the context of plane plasticity by Nye and Taylor [22]. We note that the asymptotic solution implied by (27) is not well ordered in the vicinity of the nose $x = L$, due to the divergence of the free-surface gradient here. When $L - x = O(1)$ [which is small compared to the $O(t^{2/3})$ values of L and x in the bulk solution], we have h and Y both $O(1)$ and we can no longer neglect Y in the yield condition (23b). Thus there is a boundary layer at $x = L$ in which Eq. (23) should be solved in its entirety. The derivation of this boundary layer solution is given in Ref. [19, Chapter 7]; however, the boundary layer has a negligible contribution to the volume of the mound, $V(h_0)$, and thus does not effect the leading-order scalings.

As we approach the steady state, we can no longer assume $Q_\alpha \ll 1$, but we can instead use an expression for Q_α based on $G \gg 1$, (8). Further, assuming $\mathrm{Bi} \ll 1/\hat{h}_\alpha^2$, we find that, to leading order

$$Q_\alpha = \frac{\hat{h}_\alpha^3 G}{12} + \ldots = \frac{h_0}{H_0} + \ldots, \tag{32}$$

where $H_0 = 12\hat{L}_\alpha/\hat{h}_\alpha^3$ again denotes the value of h_0 which drives a unit leakage flux, resulting in the steady state. Substituting $Q_\alpha = h_0/H_0$ and (28), we can integrate (26) to find

$$\frac{\mathrm{Bi}\,t}{H_0^3} = \log\left(\frac{1}{1-h_0/H_0}\right) - \frac{h_0}{H_0} - \frac{1}{2}\left(\frac{h_0}{H_0}\right)^2 + \ldots, \tag{33}$$

which again reduces to $h_0 = (3\mathrm{Bi}\,t)^{1/3}$ when h_0/H_0 is small and additionally implies that the steady state is approached exponentially as

$$\frac{h_0}{H_0} = 1 - \exp\left(-\frac{3}{2} - \frac{\mathrm{Bi}}{H_0^3}t\right) + \ldots. \tag{34}$$

The assumption that the bow wave is quasirigid at intermediate times, as used for this yield-stress-dominated regime, may not apply if Bi is very small. Specifically, the quasirigid approximation is valid provided $Y \ll h$, which implies $\mathrm{Bi}\,t^{1/4} \gg 1$ [since $h \sim (\mathrm{Bi}\,t)^{1/3}$ and $Y \sim (t/\mathrm{Bi}^2)^{1/6}$]. When $\mathrm{Bi}\,t^{1/4} \ll 1$, we instead have a viscously dominated bow wave. This immediately determines the timescale on which the viscously dominated regime transitions into the yield-stress-dominated regime: $T_t \sim \mathrm{Bi}^{-4}$.

2. Viscously dominated quasistatic regime

When the quasistatic mound is viscously dominated, we find from (23a) and (23b) that to leading order

$$Y = h + \ldots \quad \text{and} \quad \frac{1}{3}h^3\frac{\partial h}{\partial x} + h = 1, \tag{35}$$

which can be solved to find an implicit equation for the bow-wave shape, as given by Lister and Hinton [16]:

$$x = X(h_0) - X(h), \tag{36}$$

where

$$X(h) = \frac{1}{3}\left[\frac{1}{3}h^3 + \frac{1}{2}h^2 + h + \log(h-1)\right]. \tag{37}$$

Since $h,\ h_0 \gg 1$, this can be approximated by

$$h = [9(L-x)]^{1/3} = \left(h_0^3 - 9x\right)^{1/3}, \tag{38}$$

and so

$$V(h_0) = \frac{1}{12}h_0^4. \tag{39}$$

Repeating the approach used to derive (33) and (34), while the leakage flux is negligible we have

$$h_0 = (12t)^{1/4} + \ldots, \quad L \sim \frac{1}{9}(12t)^{3/4} + \ldots \tag{40}$$

as found by Lister and Hinton [16], and at later times, the approach to steady state is again exponential, now with

$$\frac{h_0}{H_0} = 1 - \exp\left(-\frac{11}{6} - \frac{3}{H_0^4}t\right) + \ldots. \tag{41}$$

This regime applies as long as $h \gg \mathrm{Bi}/|\partial h/\partial x|$ which implies $\mathrm{Bi}\,t^{1/4} \ll 1$, i.e., $t \ll T_t$ as anticipated.

3. Transitional timescales

As discussed above, for a given Bingham number and gap geometry, we may find only the yield-stress-dominated or viscously dominated regimes before reaching steady state, or there might be a transition from viscously to yield-stress-dominated behavior (see Fig. 5). To determine which occurs, we first note that the predicted transition from viscously dominated to yield-stress-dominated behavior occurs after a time $T_t \sim 1/\mathrm{Bi}^4$, but the quasistatic regime only occurs for $t \gg 1$, thus the quasistatic regime will only exhibit viscously dominated behavior if $\mathrm{Bi} \ll 1$. Next, we identify a timescale on which the steady state is approached, when the free-surface height reaches the critical value, $h_0 = H_0 \approx 12\hat{L}_\alpha/\hat{h}_\alpha^3$ (provided $\mathrm{Bi} \ll 1/\hat{h}_\alpha^2$). If we have $\mathrm{Bi} \geqslant O(1)$, then the behavior is yield-stress dominated throughout the evolution to the steady state, and hence the timescale on which the steady state is reached is given from (31) by $T_y \approx H_0^3/(3\mathrm{Bi}) \approx 576\hat{L}_\alpha^3/(\hat{h}_\alpha^9\mathrm{Bi})$. If, on the other hand, we assume that the behavior is viscously dominated throughout the evolution to the steady state, then this free-surface height is reached on a timescale given from (40) by $T_v \approx H_0^4/12 \approx 1728\hat{L}_\alpha^4/\hat{h}_\alpha^{12}$. Thus, there will be no transition to yield-stress-dominated behavior if the time at which the transition occurs is equal to or larger than the time at which steady state is reached, $T_t \geqslant T_v$, which occurs for $\mathrm{Bi} \lessapprox \hat{h}_\alpha^3/(12^{3/4}\hat{L}_\alpha)$. Hence, the quasistatic regime is yield-stress-dominated throughout the evolution to the steady state if $\mathrm{Bi} \geqslant O(1)$, is viscously dominated throughout the evolution to the steady state if $\mathrm{Bi} \lessapprox \hat{h}_\alpha^3/(12^{3/4}\hat{L}_\alpha)$, and exhibits a transition from viscously to yield-stress-dominated behavior if $\hat{h}_\alpha^3/(12^{3/4}\hat{L}_\alpha) \ll \mathrm{Bi} \ll 1$.

Figure 5 shows how h_0 evolves as a function of time, comparing the full numerics with the quasisteady prediction given by (26) for the specific case of $\hat{h}_\alpha = 0.1$ and $\hat{L}_\alpha = 0.5$, showing excellent agreement in the regime of validity, $t \gg 1$. The gradient indicators show the appropriate power law for the yield-stress-dominated (1/3) and viscously dominated (1/4) regimes, and the predicted timescales on which the steady state is reached are indicated by vertical lines in Figs. 5(a) and 5(c). Figure 5(b) shows the case of $\mathrm{Bi} = 0.01$, which lies in the regime in which a transition between viscously dominated and yield-stress-dominated behavior is predicted before the steady state is reached. The numerics show that such a transition does indeed take place and occurs around the predicted time $t = T_t \sim 1/\mathrm{Bi}^4$.

C. The intermediate regime for a Herschel-Bulkley fluid

Finally, while the full analysis in the sections above could be carried out for the Herschel-Bulkley model, we instead choose to present only the key predicted scalings in the early and intermediate regime. As noted in Sec. V A, the early-time scaling does not depend on N, and thus we again have $h - 1 \sim L \sim t^{1/2}$.

At the intermediate times for which $t \gg 1$ but the leakage flux is still small, $Q_\alpha \ll 1$, we have the possibility of viscously dominated and yield-stress-dominated regimes. For the former we have $Y \sim h$ and the balance between slumping and advection terms in (3) requires

$$h^{2+2/N}/L^{1/N} \sim h, \tag{42}$$

which, combined with the volume condition, $hL \sim t$, implies

$$h \sim t^{1/(N+3)} \text{ and } L \sim t^{(N+2)/(N+3)}. \tag{43}$$

On the other hand, if the behavior is yield-stress dominated, then the yield condition implies

$$h \sim \frac{\mathrm{Bi}}{h/L}, \tag{44}$$

and the predicted scaling is the same as for the Bingham fluid, namely

$$h \sim (\mathrm{Bi}\, t)^{1/3} \text{ and } L \sim (t^2/\mathrm{Bi})^{1/3}. \tag{45}$$

These scalings [Eq. (45)] are to be expected since any shear thinning (or thickening) should not enter the leading-order solution when the yield stress dominates the viscous stresses. As with the Bingham case, the viscously dominated behavior can only be observed for $\mathrm{Bi} \ll 1$ and only before a transition to yield-stress-dominated behavior occurs due to the surface slope becoming sufficiently shallow, which occurs when $\mathrm{Bi}\, t^{N/(N+3)} \sim 1$ (unless the steady state is reached on a shorter timescale than the timescale implied by this condition).

These scaling predictions are illustrated by comparison with numerical computations for the complete system (Sec. IV) with $N = 0.5$. In Fig. 6 we plot the difference between the dimensionless height of fluid at the scraper and in the far field, $h_0 - 1$, as a function time. In the first case with $\mathrm{Bi} = 10$ [Fig. 6(a)], we observe the early time dependence ($\sim t^{1/2}$) transitions to the yield-stress-dominated regime ($\sim t^{1/3}$) and the system approaches a steady state. When the dimensionless yield stress is much lower [$\mathrm{Bi} = 0.001$, Fig. 6(b)] the initial evolution exhibits the same time dependence ($\sim t^{1/2}$) but it transitions to a viscously dominated state ($\sim t^{1/3.5}$) which then subsequently evolves to a steady state.

VI. COMPARISON TO EXPERIMENTS

To investigate the validity of our shallow-layer theory for scraping of a layer of viscoplastic fluid, we have conducted experiments with a model yield-stress fluid. The methodology and results of these experiments are detailed in the following sections.

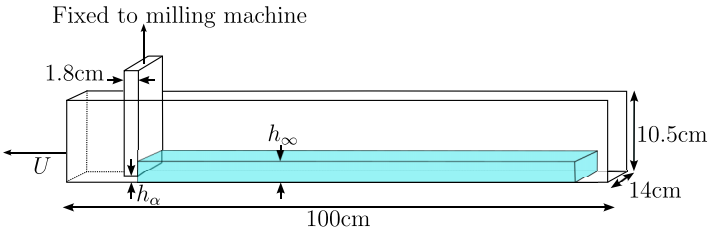

FIG. 9. Schematic of experiment configuration. The cuboidal scraper is fixed to the stationary milling machine head, while the tank containing a layer of hair gel is fixed to the bed of the machine, which can translate at uniform velocity, U. The scraper fits snugly in the channel, with the gaps on either side being approximately 0.1 mm.

A. Methodology

1. Experimental configuration

The configuration of the experiments is shown in Fig. 9. The channel (clear acrylic) was mounted on the table of a Bridgeport milling machine, while the scraper was attached to the milling machine head. The machine has a motorized bed, allowing for linear translation of the table at a range of speeds (≈0.4–8.5 mm/s) while the head (and hence scraper) remains stationary. The bed can also be raised vertically, allowing for control over the size of the gap under the scraper. To prepare the initial uniform layer thickness, a hand-held scraper was used to remove fluid above a fixed height. Still images were taken at fixed time intervals using a Canon EOS 250D camera with a timer-controlled automatic shutter trigger. The camera was positioned on a tripod in front of the scraper, which is stationary during the experiments, at a distance of approximately 70 cm from the tank. Finally, for one of the experiments, a dial indicator was mounted at the back of the scraper (see Fig. 13) to check for any deflection of the scraper. This dial indicated a maximum deflection of less than 0.05 mm and so the scraper is well represented by a static vertical boundary as assumed in the shallow-layer theory.

2. Materials

For our model yield-stress fluid we used a commercially available hair gel (Enliven Hair Gel Extreme, hold 4). Tests were carried out in a Kinexus ultra+ rotational rheometer (Malvern Instruments, Worcestershire, United Kingdom) using parallel plates of diameter 40 mm and gap 1 mm to measure the steady-state flow curve of the material. Shear-rate controlled tests were carried out for shear rates stepped up and down between 10^{-4} s^{-1} and 30 s^{-1} and amplitude controlled oscillatory measurements were taken for strains between 10^{-4} and 5 at a fixed frequency of 1 Hz. To mitigate the effects of slip on the measurements, P400 grit sandpaper was glued to the surfaces of the parallel plates. Figure 10(a) shows results for two separate up- and down-stepped shear-rate controlled tests, separated by a 100-s rest period, demonstrating that the rheology of the material is well fitted by a Herschel-Bulkley constitutive rule, with $\tau_c = 70$ Pa, $K = 80$ Pa s^N, and $N = 0.25$. Apart from at very low strain rates, the results show excellent agreement both between the up- and down-stepped tests, and between the two tests separated by the period of rest, indicating that the material does not exhibit any significant thixotropy. The large yield stress of the hair gel poses a challenge for measuring an accurate volume, and hence density, of the material. The density was found to be close to that of water, namely in the range 1000 ± 50 kg m^{-3}, and hence we take the value of 1000 kg m^{-3} in the absence of more precise volume measurements. Figure 10(b) shows the storage modulus, G', and the loss modulus, G'', as a function of strain. At low strains the material behaves like a linear viscoelastic solid, as evidenced by approximately constant values of both G' and G''. At higher strains, the storage modulus decreases dramatically, and eventually falls below the loss modulus, indicating a transition to a fluid regime. The beginning of this transition roughly

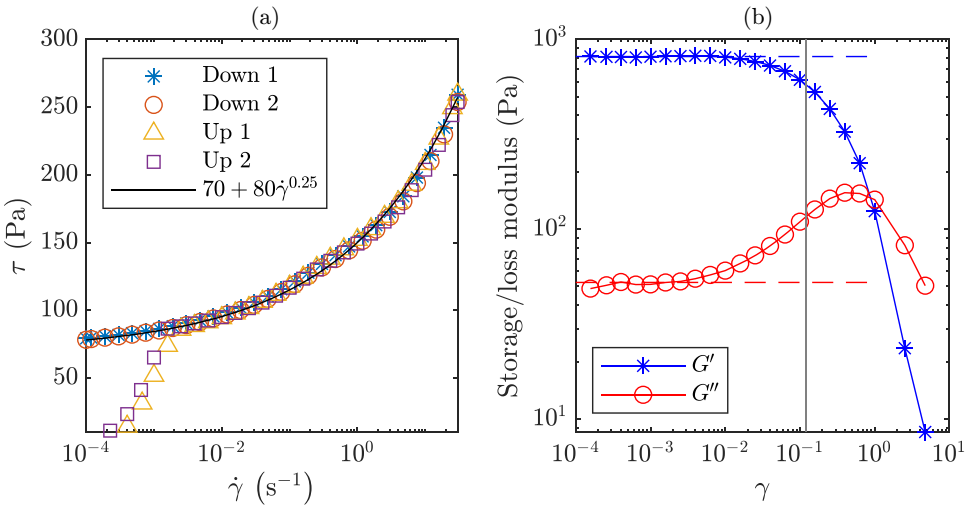

FIG. 10. Hair gel rheometry. (a) Steady-state flow curve for the commercial hair gel used in the experiments. Data (symbols) is shown for two up- and down-, shear-rate stepped tests, separated by a 100-s rest period. The solid black line indicates the flow curve for a Herschel-Bulkley constitutive law with $\tau_c = 70$ Pa, $K = 80$ Pas^N, and $N = 0.25$. (b) Storage modulus, G' (blue stars), and loss modulus, G'' (red circles), as functions of strain. The dashed blue and red lines indicate the values 813 Pa and 52.5 Pa, respectively, obtained by averaging G' and G'' over low strains ($\gamma < 10^{-2}$). The vertical gray line indicates the critical strain, $\gamma = 0.12$, at which the stress attains the yield stress, $G'\gamma = \tau_c = 70$ Pa, as obtained from the Herschel-Bulkley fit.

corresponds to the critical strain, $\gamma = 0.12$, where the stress is equal to the yield stress, $\tau_c = 70$ Pa. The average value of the storage modulus, G', over the linear viscoelastic regime (averaged over $\gamma < 10^{-2}$) is 813 Pa, while at the critical strain (i.e., at yielding) it takes the value of 578 Pa. We will discuss the relative significance of elastic effects in Sec. VI C.

To reduce the number of bubbles present in the sample, each bottle of hair gel was spun in a lathe at 2000 rpm, resulting in the bubbles converging to the center of the bottle. Inevitably some bubbles were reintroduced to the fluid in the depositing and scraping of the layer. These were seen as a convenience for visualizing the flow within the layer, and represent a sufficiently small volume fraction that we do not anticipate they had a significant impact on the rheology or dynamics of the flow.

B. Accounting for slip

Wall slip is a feature commonly reported for yield-stress fluids [23–26] and was identified in our experiments through two observations. First, the thickness of the residual layer behind the scraper (in the absence of an instability we detail in Sec. VI D) was typically uniform and equal to the gap height (see Fig. 11), which is consistent with the fluid being unyielded under the scraper, translating with the bottom boundary and slipping against the underside of the scraper. Second, small bubbles which are close to the bottom of the tank can be seen to move relative to the tank while not moving significantly relative to one another (see Fig. 11), indicating slip against the bottom of the tank. We thus introduce the effects of slip into the theory detailed in Secs. II–V.

Among experimental studies of wall slip of viscoplastic fluids, of particular relevance to our experiments are the studies of Piau [24] and Daneshi *et al.* [26], who characterize the slip of Carbopol solutions (a key ingredient in commercial hair gels) against glass and plexiglass surfaces, for different concentrations and yield stresses of solution. In both cases the data is well charaterized

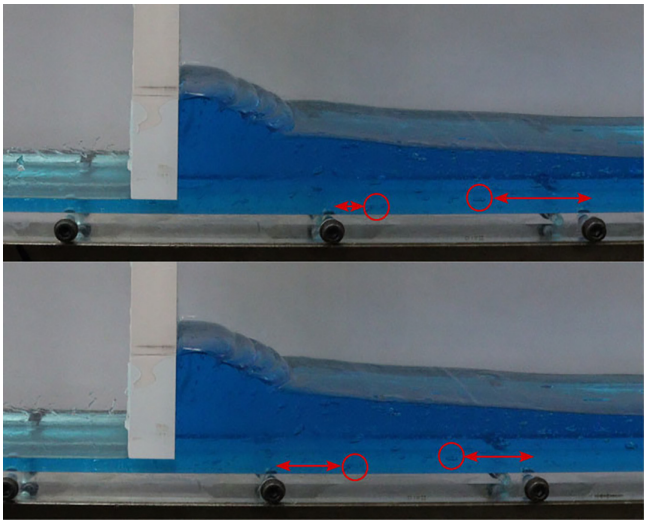

FIG. 11. Evidence of wall slip in the scraping experiments. Two images from Test IV, taken 50 s apart. The residual layer behind the scraper has a uniform thickness set by the gap height, suggesting that the fluid is slipping against the underside of the scraper. The red circles indicate two bubbles that are close to the bottom of the tank but have moved relative to the tank (the red arrows indicate the distance of the bubbles to the bolts, which are moving with the tank), indicative of slip at the base.

by a slip velocity law of the form

$$U_s = \beta \max(\tau - \tau_s, 0)^m, \tag{46}$$

where U_s is the slip velocity of the fluid relative to the boundary, τ is the shear stress at the boundary, τ_s is a slip yield stress, and β and m are parameters which, along with τ_s, can depend on the concentration of the Carbopol solution. Such a slip law has been considered for shallow flows of viscoplastic fluids in Refs. [27,28]. Daneshi *et al.* [26] found the exponent, m, to be 1.04 ± 0.06, and hence well represented by a linear relationship, $m = 1$. Piau [24] also found that the exponent was close to one for smooth surfaces such as plexiglass but could be greater than 2 for rougher surfaces (machined chromium). Given this evidence, and for simplicity, we choose a linear relationship, $m = 1$, for our model. For the slip yield stress, τ_s, both studies found a strong dependence on the yield stress of the fluid, with larger yield stresses resulting in larger slip yield stresses. However, the specific relationship varied significantly between the studies. Daneshi *et al.* [26] found that the behavior was well characterized by a linear relationship, $\tau_s = (0.18 \pm 0.02)\tau_c$, while Piau [24] found that the ratio τ_s/τ_c varied between 0.009 and 0.24. We choose to use a value at the lower end of this range, $\tau_s = 0.01\tau_c$, for two reasons. First, Piau [24] reports a value of $\tau_s = 0.07$ Pa for a sample with $\tau_c = 75$ Pa, which is close to the yield stress of our fluid (while the samples used by Daneshi *et al.* [26] reach a maximum yield stress of 32 Pa). Second, we observe slip occurring at relatively shallow free surface slopes (and hence low basal shear stresses). The constant of proportionality, β, also varies significantly with concentration and between studies. Combining the results of Daneshi *et al.* [26] and Piau [24], we find a range of between 2.2×10^{-6} m s^{-1}Pa^{-1} and 6.0×10^{-1} m s^{-1}Pa^{-1}, with the upper limit corresponding to low concentrations ($\leqslant 0.1\%$) of Carbopol, reported by Daneshi *et al.* [26], and the lower limit corresponding to high concentrations, reported by Piau [24]. We choose to use the value $\beta = 1.6 \times 10^{-5}$ m s^{-1}Pa^{-1}, which approximately corresponds to the value reported by Piau [24] for the 75 Pa yield-stress sample.

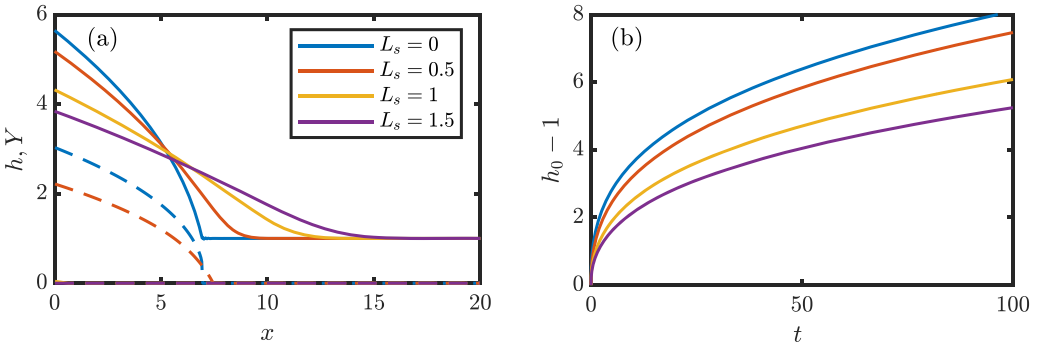

FIG. 12. (a) Free-surface profiles, h (solid), and yield-surface profiles, Y (dashed), from numerical solutions at $t = 20$ with $\mathrm{Bi} = 1$, $N = 0.25$, $\hat{h}_\alpha = 0$, and a selection of dimensionless slip-lengths, L_s (see legend). The yield surface for $L_s = 1$ and $L_s = 1.5$ are both at $Y = 0$. (b) Increase in height immediately upstream of the scraper, $h_0 - 1$, as a function of time, t, for the same parameters shown in (a).

Under the lubrication model, the magnitude of the basal shear stress, τ, is given by

$$\tau = \rho g h \left| \frac{\partial h}{\partial x} \right|. \tag{47}$$

Thus, to introduce slip into our model, we replace the bottom no-slip boundary condition, $u = -U$, with

$$u = -U + \beta \max\left(\rho g h \left| \frac{\partial h}{\partial x} \right| - 0.01\tau_c, 0 \right). \tag{48}$$

After nondimensionalization, and dropping hats from the new variables, this can be written as

$$u = -1 + U_s = -1 + L_s \max\left(h \left| \frac{\partial h}{\partial x} \right| - 0.01\mathrm{Bi}, 0 \right) \text{ at } z = 0, \tag{49}$$

where U_s is the dimensionless slip velocity and L_s is the dimensionless slip length, given by

$$L_s = \frac{\beta\mu}{h_\infty} = \frac{\beta K (U/h_\infty)^{N-1}}{h_\infty}. \tag{50}$$

The parameter $\mu = K(U/h_\infty)^{N-1}$ is the typical viscosity for the Herschel-Bulkley model, and we use the terminology "slip length" to reflect the fact that $\beta\mu$ is a length, which becomes nondimensionalized by h_∞ in the definition of L_s. With this alteration to the basal boundary condition, the evolution equation for h [Eq. (3)] gains a term, becoming

$$\frac{\partial h}{\partial t} = \frac{\partial}{\partial x}\left\{ (1 - U_s)h - \frac{N[(2N+1)h - NY]}{(N+1)(2N+1)} Y^{1+s} \left| \frac{\partial h}{\partial x} \right|^s \right\}, \tag{51}$$

with Y defined as before. The effect of slip on the shape of the predicted free-surface profile and on the evolution of the height of the mound is shown in Fig. 12 for the particular case of $\mathrm{Bi} = 1$, $N = 0.25$, and no leakage flux, $\hat{h}_\alpha = 0$. In Fig. 12(a) we see that the inclusion of slip reduces the gradient of the free surface at the nose [although the gradient discontinuity remains, due to the nonsmoothness of the maximum function in (49)]. The horizontal extent is thus increased and the height decreased. Figure 12(b) indicates that the excess height of the mound follows the same trend with time but is reduced as the slip length is increased. Another feature we observe is that the yield surface, Y, can vanish over the entirety of the mound for sufficiently large slip lengths. This may seem contradictory since it suggests the mound is deforming despite being unyielded

TABLE I. Dimensionless parameters and typical length and timescales for the five scraping experiments. The dimensionless parameters are the Bingham number, Bi, the dimensionless gap height, $\hat{h}_\alpha$, the dimensionless slip length, L_s, and the aspect ratio, $\epsilon = h_\infty/\mathcal{L}$.

Test	Bi	$\hat{h}_\alpha$	L_s	ϵ	$\mathcal{L}$ (cm)	$\mathcal{T}$ (s)
Test I	0.91	0.07	0.15	0.78	1.30	1.5
Test II	1.93	0.30	1.40	0.37	2.70	63.9
Test III	1.82	0.03	0.58	0.20	10.2	96.6
Test IV	2.29	0.30	1.20	0.16	12.9	303.8
Test V	2.29	0.03	1.20	0.16	12.9	303.8

everywhere; however, this can be rationalized as in Refs. [17,27] by showing that the fluid remains above the yield stress when higher orders are included in the asymptotic expansion.

When $\hat{h}_\alpha \neq 0$ we should also include slip in the model of leakage flux under the scraper. This can be done (e.g., see Lawal *et al.* [20]), in principle, by including further regimes in the analysis of Sec. III, dependent on whether, and in which direction, the fluid is slipping at the top and bottom of the thin gap. However, this results in a large number of possible regimes and a rather complicated model for the flux under the scraper. Rather than taking this approach, we instead appeal to the experimental observation that the residual layer is typically uniform and of thickness given by the gap height (see Fig. 11). Since the dimensionless thickness of the residual layer sufficiently far downstream of the scraper is equal to the dimensionless leakage flux, this is consistent with a particular regime in which the fluid is unyielded in the gap, and slipping only on the upper surface (giving a dimensionless flux equal to the gap height). Thus, when computing shallow-layer solutions to compare to the experiments, we use the constant value $Q_\alpha = \hat{h}_\alpha$ for the dimensionless leakage flux.

C. Dimensionless parameters

To summarize, for the material parameters of the fluid, we take $\tau_c = 70$ Pa, $K = 80\,\mathrm{Pa\,s}^N$, $N = 0.25$, and $\rho = 1000\,\mathrm{kg\,m}^{-3}$. The storage modulus was measured to be 813 Pa in the linear-viscoelastic regime and 578 Pa at yielding. For the model of slip, we take $\tau_s = 0.7$ Pa and $\beta = 1.6 \times 10^{-5}\,\mathrm{m\,s}^{-1}\,\mathrm{Pa}^{-1}$. The initial layer thickness was set as 1 cm (Tests I and II) and 2 cm (Tests III–V). The scraper velocity was varied between approximately 0.4 mm s^{-1} and 8.5 mm s^{-1}, and the gap height between approximately 0.6 and 6 mm. After nondimensionalizing according to Sec. II we obtain the dimensionless parameters shown in Table I for the five experiment runs. Also shown are the typical length and timescales, $\mathcal{L}$ and $\mathcal{T}$.

The significance of inertia in the shallow-layer governing equations is measured by a modified Reynolds number [1], $\epsilon\mathrm{Re}$, where

$$\mathrm{Re} = \frac{\rho U^2}{K(U/h_\infty)^N}, \qquad \text{and} \qquad \epsilon = h_\infty/\mathcal{L}. \tag{52}$$

For the parameters of our experiments, this quantity varies between a minimum of 9.1×10^{-7} for Tests IV and V, and a maximum of 7.3×10^{-4} for Test I, indicating that our experiments are conducted in a regime for which inertia can be safely neglected.

To determine the significance of elasticity in the experiments, we wish to compare an elastic relaxation time, t_e, to the typical timescale of the flow, $\mathcal{T}$, defining a Deborah number, $\mathrm{De} = t_e/\mathcal{T}$. When the Deborah number is small, elastic stresses relax quickly, relative to the timescale of the experiment, and can be neglected. There are multiple ways of defining such an elastic timescale [29, p.234] although there is no clear consensus in the scientific literature. One choice which has been used for power-law and Herschel-Bulkley fluids [29–31] is given by $(K/G')^{1/N}$ where G' is

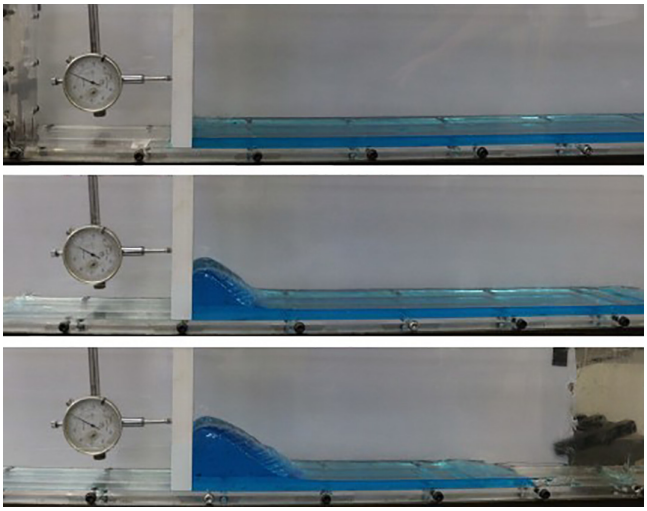

FIG. 13. Typical images from a scraping experiment (Test I). The dial indicator behind the scraper is used to test for any deflection of the scraper.

either measured in the linear-elastic regime [30] or near yielding [31]. For our material properties this gives an elastic timescale in the range 9.4×10^{-5} s $< t_e < 3.7 \times 10^{-4}$ s, which is significantly smaller than the timescales of our experiments (see Table I), resulting in Deborah numbers smaller than 2.4×10^{-4}. Another way to define an elastic timescale is $t_e = \mu/G'$ [29, p. 351]. In this case, t_e depends on the experimental parameters and, using the value of G' at yielding, the Deborah number is found to vary between 8×10^{-3} (for Tests IV and V) and 0.1 (for Test I). Thus we anticipate that our experiments are carried out in a regime in which elastic effects are largely negligible.

Finally, due to the presence of a free surface in our flow, surface tension effects could also be present in the experiments. To determine the significance of these effects we consider the capillary length, $l_c = (\sigma_t/\rho g)^{1/2}$, where σ_t is the surface tension of the fluid. For length scales, $\mathcal{L}$, below the capillary length we anticipate surface tension effects to be significant, while on significantly larger length scales they will be negligible. Alternatively, we can define the Bond number, $\mathrm{Bo} = \rho g \mathcal{L}^2/\sigma_t = \mathcal{L}^2/l_c^2$, which measures the relative sizes of gravitational and capillary stresses. Like the elastic timescale, surface tension is difficult to define and measure for a yield-stress fluid [31–34]. These previous studies have typically reported a value for Carbopol slightly below the surface tension of water (0.072 Nm^{-1}), in the range ≈0.05–0.07 Nm^{-1}. However, our commercial hair gel contains a number of other ingredients such as polyvinylpyrrolidone and triethanolamine, which could act to alter the surface tension significantly. Both of these ingredients reduce the surface tension of water when in solution [35,36], thus we report the typical capillary length and corresponding Bond numbers for a value of $\sigma_t = 0.07$ Nm^{-1}, noting that these correspond to a generous upper limit for the significance of surface tension effects in our experiments. This gives a capillary length of $l_c \approx 2.7$ mm and thus a Bond number that varies between 23 (Test I) and 2300 (Tests IV and V), indicating that surface tension is not a significant factor upstream of the scraper in our experiments.

D. Results and discussion

Figure 13 shows a selection of three typical images obtained from an experiment (Test I shown). We note that the experiments are qualitatively consistent with those reported by Maillard *et al.* [6]. Namely, upstream of the scraper, a mound of growing volume forms which has a roughly triangular shape, is approximately uniform across the channel, and exhibits undulations on the

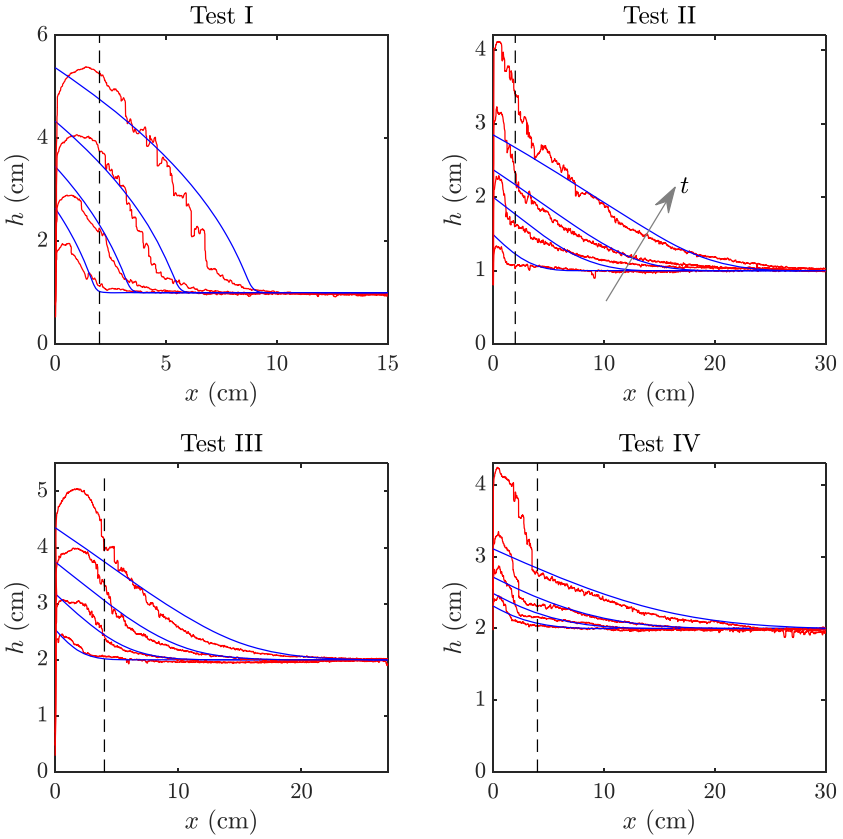

FIG. 14. Comparison of surface profiles from experiments (red) and shallow-layer theory (blue). The panels show profiles at a selection of times from four different experiments, for which the dimensionless parameters are given in Table I. The profiles shown correspond to the following dimensionless times (increasing from bottom to top as indicated for Test II): (Test I) $t = 1.4, 4.1, 9.4, 20$; (Test II) $t = 0.55, 2.5, 5.1, 10$; (Test III) $t = 0.041, 0.21, 0.50, 0.99$; and (Test IV) $t = 0.045, 0.11, 0.24, 0.60$. The vertical dashed line indicates $x = 2h_\infty$, to the left of which we anticipate the shallow-layer theory to fail.

upper surface. In the absence of an instability discussed later, the residual layer downstream of the scraper is uniform and equal to the gap height. We do not observe the 10% increase in the residual layer compared to the gap height reported by Maillard *et al.* [6]. They attributed this to elastic effects, though in the theory of this paper it could potentially result from enhanced flux under the scraper due to the hydrostatic pressure difference between the front and back of the scraper. Notably, however, their experiments used a short scraper ($L_\alpha \ll h_\alpha$) and relatively large gaps between it and the underlying plane, meaning that our theory may not be directly applied. To compare with the predictions of shallow-layer theory, we extract the free-surface profiles from these raw images by first cropping the image to a 3000×1000 pixel region containing the hair-gel layer before performing a sequence of transformations to adjust for perspective and lens distortion effects and extracting the free surface as a contour of saturation level (at a value of 0.8). Further details of this methodology can be found in Ref. [19, Chapter 7].

Figure 14 shows free-surface profiles at a selection of four times from Tests I–IV, compared against the corresponding shallow-layer predictions. These show reasonable agreement, particularly given that we have not introduced any fitted parameters and the aspect ratio, ϵ, is not especially small in any of the examples, ranging between 0.16 and 0.78 (see Table I). By comparison to Figure 12(a)

we can see that the agreement would be significantly worse without the inclusion of slip in the model. For Tests II–IV, the model without slip ($L_s = 0$) would fail to capture the convexity at the front of the mound, and in Tests II and IV ($L_s = 1.4$ and 1.2, respectively), the length of the mound would be significantly underestimated. Excluding a region close to the scraper, which we discuss later, the weakest agreement is for Test I, which corresponds to the experiment with the largest aspect ratio, $\epsilon = 0.78$, smallest Bond number, $\mathrm{Bo} = 23$, and largest Deborah number, $\mathrm{De} = 0.1$. Hence this experiment could be being more strongly effected by nonshallow, elastic, or surface tension effects.

One notable discrepancy is that the areas under the curves do not agree between experiments and theory, typically being larger in the experiments than the theoretical profiles. This could be due to discrepancies between the leakage flux used in the model and occurring in the experiment, but we anticipate this effect to be minor, since we are able to observe the uniform layer behind the scraper in the experiments (except for Test II which features an instability behind the scraper as discussed below). Rather, we believe this disagreement arises primarily due to nonplanarity of the experiments and the image processing method used to distinguish the free surface. First, as can be seen in the second panel of Fig. 13, the free surface may dip at the center of the tank, resulting in the free surface at the tank sides being larger than the average value across the tank, causing the area under the extracted experimental free surface to be larger than expected through conservation of mass. Second, even where the free surface does not dip at the center of the tank, as the mound grows, regions of the upper surface visible in the images can become darker and eventually reach the saturation threshold required to be identified with the free surface in the image processing method. Again this would result in an overestimation of the free-surface height and hence an exaggeration of the area under the curve.

The discrepancy between the theoretical and experimental profiles is generally greatest in a region close to the scraper. This is to be anticipated since, in the shallow-layer theory, vertical velocities are assumed small relative to the horizontal velocities, whereas they must become of the same magnitude at the scraper where there is a stagnation flow against the no-penetration boundary. The horizontal extent of the region where the vertical velocity becomes non-negligible is $O(\epsilon)$ in the scaled shallow-layer theory or $O(h_\infty)$ in dimensional coordinates. We hence indicate the horizontal positions corresponding to $x = 2h_\infty$ by dashed lines in Fig. 14, demonstrating that much of the discrepancy between experiments and theory can be attributed to this $O(h_\infty)$ region from the scraper, where shallow-layer theory fails.

We note two further interesting observations from the experiments. First, the free surface upstream of the scraper undergoes a buckling or wrinkling instability also observed by Maillard *et al.* [6]. These can be seen in the extracted surface profiles in Fig. 14 but perhaps are more clearly seen in the raw images in Figs. 11 and 13. This instability cannot be described through shallow-layer theory, since the wavelength of the resulting wrinkles is on the order of the height of the layer and perhaps arises through elastic or plastic buckling of an unyielded layer of fluid at the free surface. Indeed, similar surface features are seen in fully two-dimensional numerical simulations of a slumping slender vertical block of viscoplastic fluid under gravity with a small but finite Reynolds number [37], suggesting the instability can plausibly be understood as an effect of nonshallowness, without the need for additional physics such as surface tension or elasticity. A second instability can be observed in the layer downstream of the scraper for sufficiently slow speeds and thin gaps under the scraper, resulting in a periodic ripple pattern of a reasonably well defined wavelength behind the scraper (see Fig. 15). The pattern formed is reminiscent of the washboard instability where an inclined plate towed over a layer of viscoplastic fluid can become unstable to vertical oscillations, resulting in a periodic pattern behind the scraper [7]; however, this mechanism is not applicable to our instability, since the scraper is rigid and not free to lift vertically or deflect horizontally. It appears the wavelength of the pattern is set by the gap size, with the two panels in Fig. 15 corresponding to a factor of 5 difference in gap size and exhibiting a similar scaling between the resulting wavelengths. We do not believe the upstream and downstream instabilities are connected since the wavelength of the pattern downstream does not appear to be related to the

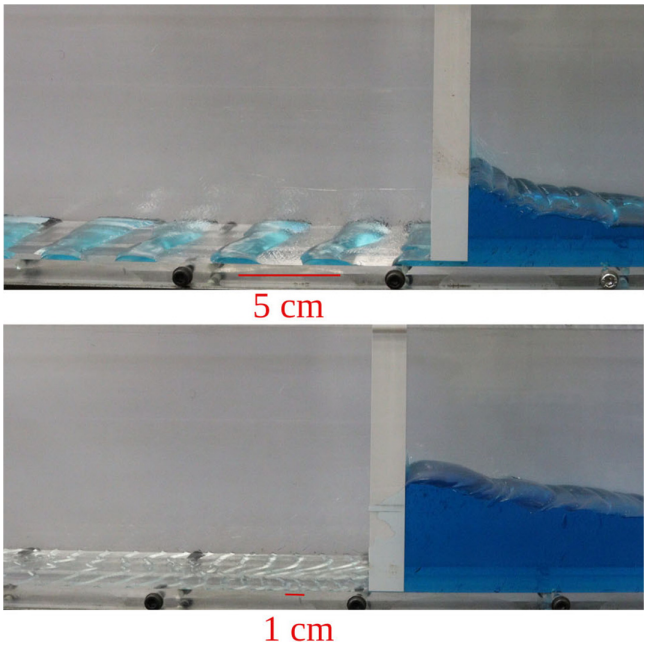

FIG. 15. The instability observed behind the scraper for slow speeds and narrow gaps. The images are from Tests II (top) and V (bottom), with dimensional gap sizes, $h_\alpha = 3$ and 0.6 mm, respectively, and speed, $U \approx 0.4$ mm/s, for both. The red lines and text indicate a typical scale for the wavelength of the instability.

wavelength upstream, and because the pattern upstream of the scraper is approximately stationary in the frame of the scraper, thereby not producing any periodic behavior at the leading edge. We are not currently able to provide a definite mechanism for this instability, which would warrant further experiments to detail the dependence on scraper velocity and gap size more fully, as well as an exploration of the further effects of material properties notably including yield stress and slip. An observed pinching-off of a slightly reduced layer height behind the scraper, and the eventual dewetting of the base between the ripples suggests that surface tension could be important in the process downstream of the scraper.

VII. CONCLUSIONS

We have used lubrication theory to predict the evolution of the free surface of a layer of viscoplastic fluid when scraped by an infinitely wide scraper with a small gap underneath. The motion of the scraper leads to a buildup of fluid upstream forming a deepening mound, while a thin layer flows under the scraper. At early times the depression of the free surface behind the scraper is a reflection of the elevation ahead of the scraper, which grows as $t^{1/2}$ in height and length. The leakage flux varies according to the hydrostatic pressure difference between the upstream and downstream edges of the scraper, so that a steady state is eventually reached, though only after very large times when the gap under the scraper is small. On the approach to this steady state there are three regimes, the initial early-time adjustment, followed by a quasisteady intermediate-time regime, before an exponential approach to the steady state. At intermediate times, the mound can exhibit a viscously dominated solution, for which the height and length grow as $t^{1/(3+N)}$ and $t^{(2+N)/(3+N)}$, respectively (for shear index, N), or a yield-stress-dominated regime, for which the height and length grow as $t^{1/3}$ and $t^{2/3}$, respectively. It can also start in the viscously dominated regime and transition to the yield-stress-dominated regime, before reaching steady state. After the initial adjustment of the free

surface behind the scraper, the residual layer becomes unyielded and varies very slowly in height with the slowly varying leakage flux.

To test the predictions of the shallow-layer theory, we carried out preliminary experiments using a commercial hair gel. These indicated a need to include slip into the model, after which the free-surface profiles agreed reasonably well with the theory, except for in a region close to the scraper which is not well described by shallow-layer theory due to significant vertical velocities. We observed a previously reported buckling instability of the free surface as well as a novel instability associated with the thin gap under the scraper. The results of these preliminary experiments indicate the need for additional experimental investigation, in particular to better understand the instability downstream of the scraper and to further explore the effects of material properties including yield stress and slip. Future theoretical work on the problem could involve extending the time-dependent theory given in this paper to a scraper of finite width to determine the transient dynamics of the mound in three dimensions, as it evolves to the steady-state solution given by Lister and Hinton [16].

ACKNOWLEDGMENTS

We thank A. Rust for helpful support in setting up the experiments, and the Laboratory for Complex and Non-Newtonian Flow (University of British Columbia) for the use of their rheometer. This work was carried out using the computational facilities of the Advanced Computing Research Centre, University of Bristol. This work was funded by the Engineering and Physical Sciences Research Council (EPSRC), UK (EP/R513179/1). J.J.T.-W. was further supported by EPSRC, as a National Fellow in Fluid Dynamics (EP/X028011/1). A.J.H. and J.J.T.-W. acknowledge the support of the National Environment Research Council (NE/X007197/1) and Mitacs (GR025763), through the Globalink research internship scheme.

APPENDIX A: FLOW UNDER THE SCRAPER

Under the lubrication approximation, the dimensionless shear stress under the scraper is given by

$$\tau = \mathrm{Bi} + G[z - \hat{h}_\alpha(1-\lambda_1)], \tag{A1}$$

where λ_1 is a constant of integration, chosen such that there is a yield surface at $z = \hat{h}_\alpha(1-\lambda_1)$, and the fluid is yielded between this position and the underside of the scraper. Expressions for λ_1 are given below. In combination with the constitutive law,

$$\tau = \mathrm{Bi} + (\partial u/\partial z)^N \quad (\text{where } \partial u/\partial z > 0), \tag{A2}$$

this motivates the choice of gap-scaled variables, $P = G\hat{h}_\alpha^{N+1}$ and $\mathrm{Bi}_g = \mathrm{Bi}\hat{h}_\alpha^N$. The gap-scaled leakage flux, $Q_\alpha/\hat{h}_\alpha$, then depends only on P, Bi_g, and N, not on $\hat{h}_\alpha$.

As discussed in Sec. III, depending on the size of the pressure gradient, P, we have three different flow regimes in the gap (see Fig. 2). Below we detail the ranges of validity for each regime and report the corresponding expression for the leakage flux under the scraper. For the detailed derivation of these results see Refs. [19,20].

Regime 1:

The first regime applies for $0 < P \leqslant P_1$, where $P_1 = [(N+1)/N]^N$. For this regime, the leakage flux is given by

$$\frac{Q_\alpha}{\hat{h}_\alpha} = \frac{P^s}{(s+1)(s+2)}\left\{(s+2)\lambda_1^{s+1} - \left[\lambda_1^{s+2} - (\lambda_1-1)^{s+2}\right]\right\}, \tag{A3}$$

where λ_1 is the solution to the equation

$$\lambda_1^{s+1} - (\lambda_1 - 1)^{s+1} = \frac{s+1}{P^s}. \tag{A4}$$

Regime 2:
The second regime applies for $P_1 < P \leqslant P_2$, where P_2 is given implicitly by

$$P_2 - [(s+1)P_2]^{\frac{1}{s+1}} = 2\mathrm{Bi}_g. \tag{A5}$$

In this regime the leakage flux is

$$\frac{Q_\alpha}{\hat{h}_\alpha} = 1 - \frac{P^s}{(s+1)(s+2)}\lambda_1^{s+2}, \tag{A6}$$

with λ_1 satisfying

$$\lambda_1^{s+1} = \frac{s+1}{P^s}. \tag{A7}$$

Regime 3:
The third regime applies for $P > P_2$. In this regime, there is a second yielded region, and so we can define λ_2 as the gap-scaled distance from the bottom boundary to the plug. Thus the shear stress under the gap can also be written in terms of λ_2 as

$$\hat{h}_\alpha^N \tau = -\mathrm{Bi}_g + P\left(\frac{z}{\hat{h}_\alpha} - \lambda_2\right) = \mathrm{Bi}_g + P\left[\frac{z}{\hat{h}_\alpha} - (1-\lambda_1)\right]. \tag{A8}$$

The leakage flux is given by

$$\frac{Q_\alpha}{\hat{h}_\alpha} = U_p - \frac{P^s}{(s+1)(s+2)}\left(\lambda_1^{s+2} + \lambda_2^{s+2}\right), \tag{A9}$$

where U_p is the plug velocity:

$$U_p = \frac{P^s}{s+1}\lambda_1^{s+1} = 1 + \frac{P^s}{s+1}\lambda_2^{s+1}, \tag{A10}$$

and λ_1 and λ_2 are determined from

$$\lambda_1 + \lambda_2 = 1 - \frac{2\mathrm{Bi}_g}{P} \quad \text{and} \quad \lambda_1^{s+1} - \lambda_2^{s+1} = \frac{s+1}{P^s}. \tag{A11}$$

It is insightful to report the results for a Bingham fluid ($N = s = 1$), because in this case the expressions for the flux are available explicitly in terms of the scaled pressure gradient, P, and Bingham number, Bi_g:

$$\frac{Q_\alpha}{\hat{h}_\alpha} = \begin{cases} \dfrac{1}{2} + \dfrac{P}{12} & \text{for } 0 < P \leqslant P_1, \\ 1 - \dfrac{1}{3}\sqrt{\dfrac{2}{P}} & \text{for } P_1 < P \leqslant P_2, \\ U_p - \dfrac{U_p}{3}\sqrt{\dfrac{2U_p}{P}} - \dfrac{U_p - 1}{3}\sqrt{\dfrac{2\left(U_p - 1\right)}{P}} & \text{for } P > P_2. \end{cases} \tag{A12}$$

In these expressions, the nondimensional plug velocity, U_p, is given by

$$U_p = \frac{1}{4}\left(R + \frac{1}{R}\right)^2, \text{ with } R = \sqrt{\frac{P}{2}}\left(1 - \frac{2\mathrm{Bi}_g}{P}\right), \tag{A13}$$

while the critical values of the scaled nondimensional pressure gradient are given by

$$P_1 = 2, \quad P_2 = 1 + 2\mathrm{Bi}_g + \sqrt{1 + 4\mathrm{Bi}_g}. \tag{A14}$$

From the stress under the scraper, (A1), we can immediately determine the drag force per unit width on the scraper due to the shear in the gap for any shear index. This is given, in the original

dimensionless variables, by

$$F_d = \hat{L}_\alpha(\mathrm{Bi} + \hat{h}_\alpha \lambda_1 G), \tag{A15}$$

where λ_1 is given for each of the three regimes by (A4), (A7), and (A11). In particular, in the steady state, the flow under the scraper is in the third regime and $P \gg 1$. In this case, from (A11) we have

$$\lambda_1 = \frac{1}{2} - \frac{\mathrm{Bi}_g}{P} + \ldots \Rightarrow \quad F_d = \frac{\hat{L}_\alpha \hat{h}_\alpha G}{2} + \ldots = \frac{\hat{h}_\alpha h_0}{2} + \ldots, \tag{A16}$$

where we have used $G = h_0/\hat{L}_\alpha + \ldots$, since $h_0 \gg h_b$ at steady state. This is much smaller than the force per unit width acting on the scraper due to hydrostatic pressure in the mound upstream of the scraper,

$$F_p = \int_{\hat{h}_\alpha}^{h_0} h_0 - z\, dz = \frac{h_0^2}{2} + \ldots. \tag{A17}$$

Thus the force required to push the scraper in steady state, $F = F_d + F_p$, is dominated by the hydrostatic contribution.

APPENDIX B: NUMERICAL SCHEME FOR INTEGRATING (3) AND (4)

For efficient numerical resolution of the evolving mound of fluid upstream of the scraper, we choose to restrict the computational domain to the upstream extent of the mound, $L(t)$, and scale the x coordinate by the length of the mound

$$\zeta = \frac{x}{L(t)}. \tag{B1}$$

This introduces an advection term to the equation, which becomes (taking the Bingham case, $N = 1$, for clarity)

$$h_t = \frac{1}{L}\left[\frac{1}{6L} Y^2 (3h - Y) h_\zeta + h\right]_\zeta + \frac{\zeta \dot{L}}{L} h_\zeta \equiv \frac{1}{L} q_\zeta + r, \tag{B2}$$

$$Y = \max\left(0, h - \frac{L\mathrm{Bi}}{|h_\zeta|}\right), \tag{B3}$$

where subscripts represent partial differentiation, dot represents differentiation with respect to time, and q and r are the flux and advection terms. We solve this equation numerically using the numerical scheme proposed by Balmforth *et al.* [38]. We construct an (in general) nonuniform spatial grid, $\zeta = \{\zeta^{(i)}, i = 0, \ldots, M\}$, where $\zeta^{(0)} = 0$ and $\zeta^{(M)} = 1$. This grid could be chosen to be uniform, $\zeta^{(i)} = i/M$, but, to improve resolution at the nose, we typically use the grid $\zeta^{(i)} = (i/M)^{1/p}$ where $p > 1$ is a constant, and is chosen as $p = 3$ for the majority of the results presented in this paper. Results were compared for a number of different values of M to ensure the solutions were independent of the grid resolution, and $M = 200$ was found to give well converged and resolved solutions. The one exception to the above is for the lowest value of the Bingham number, $\mathrm{Bi} = 0.001$. In this case the low yield stress results in a much shallower front of the mound and the higher resolution is not needed here. In fact, the strong concentration of grid points at the front for $p = 3$ was found to cause numerical difficulties in the time integration of this case. For this case we therefore used a uniform mesh ($p = 1$) with a larger number of points, $M = 500$. Again the solution was compared to solutions with different values of M to ensure independence of the grid choice.

Discretization of (B2) provides ODEs for $h^{(i)}$, $i = 1, \ldots, M-1$, given by

$$\dot{h}^{(i)} = \frac{2}{L} \frac{q^{(i+1/2)} - q^{(i-1/2)}}{\zeta^{(i+1)} - \zeta^{(i-1)}} + \frac{\zeta^{(i+1)} - \zeta^{(i)}}{\zeta^{(i+1)} - \zeta^{(i-1)}} r^{(i+1/2)} + \frac{\zeta^{(i)} - \zeta^{(i-1)}}{\zeta^{(i+1)} - \zeta^{(i-1)}} r^{(i-1/2)}, \tag{B4}$$

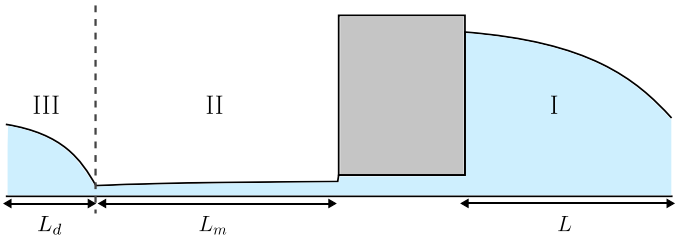

FIG. 16. Diagram showing the three different solution regions used in the numerical method.

where $q^{(i+1/2)}$ and $r^{(i+1/2)}$ are the flux and advection terms in (B2) evaluated at $\zeta^{(i+1/2)} = (\zeta^{(i)} + \zeta^{(i+1)})/2$. We have $\dot{h}^{(M)} = 0$ [with initial condition satisfying $h^{(M)} = 1$], and the flux boundary conditions provide ODEs for $h^{(0)}$ and L, via

$$\dot{h}^{(0)} = 2\frac{q^{(1/2)} - Q_\alpha}{L\zeta^{(1)}}, \quad \dot{L} = 2\frac{q^{(M-1/2)} - 1}{1 - h^{(M-1)}}, \tag{B5}$$

where Q_α is the leakage flux. These coupled ODEs are solved using a backward differentiation formula, as implemented in SciPy's "*solve_ivp*" function [39].

When integrating from $t = 0$ with an initially uniform layer of fluid, the approach above fails since $L(0) = 0$ and the transformation to the stretched variable (B1) is singular. Instead, we implement the method above on an unscaled horizontal grid (i.e., $L = 1$, $dL/dt = 0$) and a domain size chosen sufficiently large to encompass the disturbed region throughout the time period under consideration. It is then possible to use the resulting solution as an initial profile to commence further time-stepping using the method detailed above with a rescaled grid.

It is also possible to solve for the free-surface height behind the scraper, using an equivalent scheme to above. The length of the disturbed region downstream of the scraper is denoted L_d and is solved for in the same manner as L in front of the scraper. Behind the scraper there is an additional complication that occurs when the fluid behind the scraper drops to a level at which it is unyielded. The boundary condition immediately behind the scraper is given (for the Bingham case, $N = 1$) by

$$\frac{1}{6}Y^2(3h - Y)\frac{\partial h}{\partial x} + h = Q_\alpha \quad \text{at} \quad x = -\hat{L}_\alpha, \tag{B6}$$

thus, as long as $h_b \neq Q_\alpha$, we require $Y \neq 0$ and the layer to be yielded, but when h_b equals Q_α the layer must be unyielded. Thus $h_b = Q_\alpha$ constitutes a singular point of the equations which permits discontinuous derivatives, presenting numerical difficulty. Rather than attempting to integrate through this singular point, the integration is interrupted when h_b first equals Q_α. Provided the layer does not become reyielded immediately behind the scraper, after this time there are three distinct regions to the free surface (see Fig. 16): the growing mound in front of the scraper (region I); an unyielded layer behind the scraper that, in the frame of the scraper, is purely advected to the left and satisfies $h_b = Q_\alpha$ at the scraper boundary (region II); and the region downstream of the scraper that deformed in the initial stages of the problem (region III). In region I we use the numerical scheme as detailed above. In region II we define

$$\zeta_m = \frac{x + \hat{L}_\alpha}{L_m(t)} + 1, \tag{B7}$$

such that ζ_m varies between 0, at the boundary between regions II and III, and 1, at the back of the scraper. The governing equation is then given by (B2) with $\zeta \to \zeta_m$, $L \to L_m$ and $q = h$ (since the layer is unyielded throughout this region). In region III we define

$$\zeta_d = \frac{x + \hat{L}_\alpha + L_m(t)}{L_d(t)} + 1, \tag{B8}$$

which varies between 0, where region III meets the undisturbed uniform layer downstream of the scraper, and 1, at the boundary between regions II and III. The governing equation is then given by

$$h_t = \frac{1}{L_d} q_{\zeta_d} + \frac{(\zeta_d - 1)\dot{L}_d - \dot{L}_m}{L_d} h_{\zeta_d}. \tag{B9}$$

We write $h_d^{(i)}$, $q_d^{(i)}$ …, for the values of the variables at the grid points in region III, $\zeta = \zeta_d^{(i)}$ (where $0 \leqslant i \leqslant M_d$), and likewise for region II with subscript m. We then discretize the governing equation in region III exactly analogously to (B4). The equation in region II is discretized using an upwinding scheme as

$$\dot{h}_m^{(i)} = \frac{1 + (\zeta_m - 1)\dot{L}_m}{L_m} \frac{h_m^{(i+1)} - h_m^{(i)}}{\zeta_m^{(i+1)} - \zeta_m^{(i)}}. \tag{B10}$$

The conditions at the boundaries of each region then provide a set of equations analogous to (B5), providing the evolution equations for L_d, L_m, $h_d^{(M_d)}$, $h_m^{(0)}$, and $h_m^{(M_m)}$:

$$\dot{L}_d + \dot{L}_m = 2\frac{q_d^{(1/2)} - 1}{h_d^{(1)} - 1}, \quad \dot{h}_m^{(M_m)} = 2\frac{Q_\alpha - h_m^{(M_m)}}{L_m\left[1 - \zeta_m^{(M_m - 1)}\right]}, \tag{B11}$$

$$\dot{h}_d^{(M_d)} = \dot{h}_m^{(0)} = \frac{2}{L_d}\frac{h_d^{(M_d)} - q_d^{(M_d - 1/2)}}{1 - \zeta_d^{(M_d - 1)}} - \frac{\dot{L}_m}{L_d}\frac{h_d^{(M_d)} - h_d^{(M_d - 1)}}{1 - \zeta_d^{(M_d - 1)}} = \frac{1 - \dot{L}_m}{L_m}\frac{h_m^{(1)} - h_m^{(0)}}{\zeta_m^{(1)}}. \tag{B12}$$

These ODEs supplement the ODEs derived from discretization of the governing equations on the interior of each region and the full system of ODEs is again solved using the backward differentiation formula implements in SciPy's "*solve_ivp*" function [39].

Eventually the fluid becomes unyielded throughout regions II and III. We treat this as having occurred if the value of the yield height, Y, drops below a threshold value at all points in these downstream regions. After this point, we stop solving in region III and stop rescaling region II, instead allowing the solution to advect out of the numerical domain. Specifically, we continue to solve in region I as before, but in region II we set $\dot{L}_m = 0$ and

$$\dot{h}_m^{(0)} = \frac{h_m^{(1)} - h_m^{(0)}}{L_m \zeta_m^{(1)}}, \tag{B13}$$

in the scheme above. We are mostly not interested in the slow slumping of the fluid in region III, since it has no effect on the evolution of the mound upstream of the scraper. Hence, to speed up the numerical solution, we take the threshold value of Y to be not particularly small (for example $Y = 0.1$). Provided the fluid in region II is unyielded, this has no impact on the calculation of the evolution of the upstream mound, and simply means we stop solving for the slow evolution of the layer in region III slightly before this region has become completely rigid. Indeed it has previously been shown that the shallow layer model for a viscoplastic fluid can exhibit infinite stopping times [40], and so it may not even be possible to continue solving until this region becomes completely rigid.

APPENDIX C: EARLY TIME ODE

We solve the ODE (17) using a shooting method. We first write it as the system

$$\frac{d}{d\xi}\left(\hat{H}, \hat{H}', \mathcal{Y}\right) = \left[\hat{H}', \frac{3x_N^2(\hat{H} - \xi\hat{H}')}{2\mathcal{Y}(3 - 3\mathcal{Y} + \mathcal{Y}^2)}, -\frac{3x_N^2(\hat{H} - \xi\hat{H}')}{2\mathcal{Y}(3 - 3\mathcal{Y} + \mathcal{Y}^2)\hat{H}'^2}\right]. \tag{C1}$$

This system is singular at the point $\xi = 1$, and so for a given value of x_N, we integrate from $\xi = 1 - \delta$ with $\delta \ll 1$ to $\xi = 0$. Then global mass conservation $x_N^2 \int_0^1 \hat{H}\, d\xi = (1 - Q_\alpha)/\mathrm{Bi}$ provides the connection between the chosen value of x_N and the ratio $\mathrm{Bi}/(1 - Q_\alpha)$. It is then straightforward to

iteratively adjust x_N until the required value of this ratio is obtained. The leading-order forms of the dependent variables at $\xi = 1 - \delta$ are given by

$$\hat{H} = \delta + \ldots, \qquad \hat{H}' = -1 + \ldots, \qquad \text{and} \qquad \mathcal{Y} = x_N\sqrt{\delta} + \ldots. \tag{C2}$$

The numerical solutions are found to be essentially independent of $\delta \ll 1$ by comparing solutions for $\delta = 10^{-6}$, 10^{-8}, and 10^{-10}. A value of $\delta = 10^{-8}$ is taken for all calculations shown in this study.

When $\mathrm{Bi}/(1 - Q_\alpha) \ll 1$ the yield surface elevation, $\mathcal{Y} = 1$ to leading order, and we anticipate that $x_N \gg 1$. The governing equation (17) for $\hat{H} = \hat{H}_0 + \ldots$ simplifies to

$$\hat{H}_0 - \xi\hat{H}_0' = \frac{1}{3x_N^2}\hat{H}_0''. \tag{C3}$$

This equation has a solution which decays when $x_N\xi \gg 1$, given by

$$\hat{H}_0 = c_1\left[2\sqrt{3\pi}\,\mathrm{e}^{-3x_N^2\xi^2/4} - 3\pi x_N\xi\,\mathrm{erfc}\left(\frac{x_N\xi\sqrt{3}}{2}\right)\right], \tag{C4}$$

where c_1 is a constant and $\mathrm{erfc}(\cdot)$ is the complementary error function. This solution does not, however, satisfy the boundary conditions at the front ($\xi = 1$), and instead must be asymptotically matched to a solution valid in a region close to the front. This matching determines the otherwise unknown constant c_1.

The expansion close to the front (C2) illustrates that when $\delta \sim x_N^{-2}$, the height $\hat{H} \sim x_N^{-2}$. Thus we introduce variables $\hat{H} = \tilde{H}/x_N^2$ and $\zeta = x_N^2(1 - \xi)$ to investigate the dependence in that region. Since $x_N \gg 1$, we expand $\tilde{H} = \tilde{H}_0 + \ldots$, $\mathcal{Y} = \mathcal{Y}_0 + \ldots$, and find that at leading order

$$\tilde{H}_0 = \frac{\mathcal{Y}_0^2(3 - \mathcal{Y}_0)}{3}\frac{d\tilde{H}_0}{d\zeta}, \qquad \text{where} \qquad \mathcal{Y}_0 = 1 - \frac{1}{d\tilde{H}_0/d\zeta}. \tag{C5}$$

This equation may be integrated numerically and we determine that $\tilde{H}_0 \to 0.9304\exp(3\zeta/2)$ as $\zeta \to \infty$. It is this expression that provides the functional form that the solution (C4) must match as the front is approached.

To perform the matching we substitute $\xi = 1 - \zeta/x_N^2$ into (C4) and expand on the basis that $x_N \gg 1$. In this way we find that

$$\hat{H}_0 = \frac{4c_1\sqrt{3\pi}\,\mathrm{e}^{-3x_N^2/4}}{3x_N^2}e^{3\zeta/2} + \ldots = \frac{0.9304}{x_N^2}e^{3\zeta/2} + \ldots. \tag{C6}$$

To complete the asymptotic description we must impose the global mass balance (18 c). The dominant contribution is provided by the solution $\hat{H}_0$ and thus we find that

$$\frac{1 - Q_\alpha}{\mathrm{Bi}} = x_N^2\int_0^1 \hat{H}\,d\xi = x_N^2\int_0^\infty \hat{H}_0\,d\xi + \ldots = \pi x_N c_1. \tag{C7}$$

Hence we may implicitly determine the leading-order expressions for length of the current in similarity variable, x_N, and the scaled depth of the flow at the origin, $\hat{H}(0)$, in the regime $\mathrm{Bi}/(1 - Q_\alpha) \ll 1$

$$\frac{0.9304\sqrt{3\pi}}{4}x_N\exp\left(\frac{3x_N^2}{4}\right) = \frac{(1 - Q_\alpha)}{\mathrm{Bi}} \qquad \text{and} \qquad \hat{H}(0) = \frac{3 \times 0.9304}{2}\exp\left(\frac{3x_N^2}{4}\right). \tag{C8}$$

These dependencies are plotted in Fig. 7, and shown to represent the numerical solution accurately.

[1] C. Ancey and S. Cochard, The dam-break problem for Herschel-Bulkley viscoplastic fluids down steep flumes, J. Non-Newton. Fluid Mech. **158**, 18 (2009).
[2] C. C. Mei, K.-F. Liu, and M. Yuhi, Mud flow—Slow and fast, in *Geomorphological Fluid Mechanics*, edited by N. J. Balmforth and A. Provenzale (Springer, Berlin, 2001), pp. 548–577.
[3] G. Sant, C. F. Ferraris, and J. Weiss, Rheological properties of cement pastes: A discussion of structure formation and mechanical property development, Cement Concrete Res. **38**, 1286 (2008).
[4] A. B. Ross, S. K. Wilson, and B. R. Duffy, Blade coating of a power-law fluid, Phys. Fluids **11**, 958 (1999).
[5] C. Xu and N. Willenbacher, How rheological properties affect fine-line screen printing of pastes: a combined rheological and high-speed video imaging study, J. Coat. Technol. Res. **15**, 1401 (2018).
[6] M. Maillard, C. Mézière, P. Moucheront, C. Courrier, and P. Coussot, Blade-coating of yield stress fluids, J. Non-Newton. Fluid Mech. **237**, 16 (2016).
[7] I. J. Hewitt and N. J. Balmforth, Viscoplastic lubrication theory with application to bearings and the washboard instability of a planing plate, J. Non-Newton. Fluid Mech. **169-170**, 74 (2012).
[8] S. H. Emerman and D. Turcotte, A fluid model for the shape of accretionary wedges, Earth Planet. Sci. Lett. **63**, 379 (1983).
[9] C. A. Perazzo and J. Gratton, Asymptotic regimes of ridge and rift formation in a thin viscous sheet model, Phys. Fluids **20**, 043103 (2008).
[10] T. V. Ball, C. E. Penney, J. A. Neufeld, and A. C. Copley, Controls on the geometry and evolution of thin-skinned fold-thrust belts, and applications to the Makran accretionary prism and Indo–Burman Ranges, Geophys. J. Int. **218**, 247 (2019).
[11] G. S. Stockmal, Modeling of large-scale accretionary wedge deformation, J. Geophys. Res.: Solid Earth **88**, 8271 (1983).
[12] D. Davis, J. Suppe, and F. A. Dahlen, Mechanics of fold-and-thrust belts and accretionary wedges, J. Geophys. Res.: Solid Earth **88**, 1153 (1983).
[13] G. S. Stockmal, C. Beaumont, M. Nguyen, and B. Lee, Mechanics of thin-skinned fold-and-thrust belts: Insights from numerical models, in *Whence the Mountains? Inquiries into the Evolution of Orogenic Systems: A Volume in Honor of Raymond A. Price*, edited by J. W. Sears, T. A. Harms, and C. A. Evenchick (Geological Society of America, Boulder, CO, 2007).
[14] G. Simpson, Mechanics of non-critical fold–thrust belts based on finite element models, Tectonophysics **499**, 142 (2011).
[15] J. B. Ruh, B. J. P. Kaus, and J.-P. Burg, Numerical investigation of deformation mechanics in fold-and-thrust belts: Influence of rheology of single and multiple décollements, Tectonics **31**, TC3005 (2012).
[16] J. R. Lister and E. M. Hinton, Using a squeegee on a layer of viscous or viscoplastic fluid, Phys. Rev. Fluids **7**, 104101 (2022).
[17] N. J. Balmforth and R. V. Craster, A consistent thin-layer theory for Bingham plastics, J. Non-Newton. Fluid Mech. **84**, 65 (1999).
[18] N. J. Balmforth, R. V. Craster, A. C. Rust, and R. Sassi, Viscoplastic flow over an inclined surface, J. Non-Newton. Fluid Mech. **142**, 219 (2007).
[19] J. J. Taylor-West, Flows of Viscoplastic Fluids, Ph.D. thesis, University of Bristol, 2023.
[20] A. Lawal, D. M. Kalyon, and U. Yilmazer, Extrusion and lubrication flows of viscoplastic fluids with wall slip, Chem. Eng. Commun. **122**, 127 (1993).
[21] N. J. Balmforth, R. V. Craster, and R. Sassi, Shallow viscoplastic flow on an inclined plane, J. Fluid Mech. **470**, 1 (2002).
[22] J. F. Nye and G. I. Taylor, The flow of glaciers and ice-sheets as a problem in plasticity, Proc. R. Soc. Lond. A **207**, 554 (1951).
[23] H. A. Barnes, A review of the slip (wall depletion) of polymer solutions, emulsions and particle suspensions in viscometers: its cause, character, and cure, J. Non-Newton. Fluid Mech. **56**, 221 (1995).
[24] J. M. Piau, Carbopol gels: Elastoviscoplastic and slippery glasses made of individual swollen sponges: Meso- and macroscopic properties, constitutive equations and scaling laws, J. Non-Newton. Fluid Mech. **144**, 1 (2007).

[25] M. Cloitre and R. T. Bonnecaze, A review on wall slip in high solid dispersions, Rheol Acta **56**, 283 (2017).
[26] M. Daneshi, A. Pourzahedi, D. Martinez, and D. Grecov, Characterising wall-slip behaviour of carbopol gels in a fully-developed Poiseuille flow, J. Non-Newton. Fluid Mech. **269**, 65 (2019).
[27] N. J. Balmforth, Viscoplastic asymptotics and other analytical methods, in *Lectures on Visco-Plastic Fluid Mechanics*, edited by G. Ovarlez and S. Hormozi (Springer International, Cham, 2019), pp. 41–82.
[28] A. P. Dufresne, T. V. Ball, and N. J. Balmforth, Viscoplastic Saffman–Taylor fingers with and without wall slip, J. Non-Newton, Fluid Mech. **312**, 104970 (2023).
[29] R. B. Bird, R. C. Armstrong, and O. Hassager, *Dynamics of Polymeric Liquids* (Wiley, New York, 1987).
[30] L.-H. Luu and Y. Forterre, Drop impact of yield-stress fluids, J. Fluid Mech. **632**, 301 (2009).
[31] J. van der Kolk, D. Tieman, and M. Jalaal, Viscoplastic lines: printing a single filament of yield stress material on a surface, J. Fluid Mech. **958**, A34 (2023).
[32] J. Boujlel and P. Coussot, Measuring the surface tension of yield stress fluids, Soft Matter **9**, 5898 (2013).
[33] B. Géraud, L. Jørgensen, L. Petit, H. Delanoë-Ayari, P. Jop, and C. Barentin, Capillary rise of yield-stress fluids, Europhys. Lett. **107**, 58002 (2014).
[34] L. Jørgensen, M. Le Merrer, H. Delanoë-Ayari, and C. Barentin, Yield stress and elasticity influence on surface tension measurements, Soft Matter **11**, 5111 (2015).
[35] A. N. Campbell, Activity coefficients, densities, dipole moments, and surface tensions of the system triethylamine–methylethylketone–water, Can. J. Chem. **59**, 127 (1981).
[36] B. A. Noskov, A. V. Akentiev, and R. Miller, Dynamic surface properties of poly(vinylpyrrolidone) solutions, J. Colloid Interface Sci. **255**, 417 (2002).
[37] Y. Liu, N. J. Balmforth, S. Hormozi, and D. R. Hewitt, Two-dimensional viscoplastic dambreaks, J. Non-Newton. Fluid Mech. **238**, 65 (2016).
[38] N. J. Balmforth, R. V. Craster, P. Perona, A. C. Rust, and R. Sassi, Viscoplastic dam breaks and the Bostwick consistometer, J. Non-Newton. Fluid Mech. **142**, 63 (2007).
[39] P. Virtanen, R. Gommers, T. E. Oliphant, M. Haberland, T. Reddy, D. Cournapeau, E. Burovski, P. Peterson, W. Weckesser, J. Bright, S. J. van der Walt, M. Brett, J. Wilson, K. J. Millman, N. Mayorov, A. R. J. Nelson, E. Jones, R. Kern, E. Larson, C. J. Carey *et al.*, SciPy 1.0: fundamental algorithms for scientific computing in python, Nature Methods **17**, 261 (2020).
[40] G. P. Matson and A. J. Hogg, Two-dimensional dam break flows of Herschel–Bulkley fluids: The approach to the arrested state, J. Non-Newton. Fluid Mech. **142**, 79 (2007).